Acta Materialia 206 (2021) 116616

Contents lists available at ScienceDirect

Acta Materialia

journal homepage: www.elsevier.com/locate/actamat

Competing Interactions between Mesoscale Length-Scales, Order-Disorder, and Martensitic Transformation in Ferromagnetic Shape Memory Alloys

D. Salas[a], Y. Wang[a], T.C. Duong[a], V. Attari[a], Y. Ren[b], Y. Chumlyakov[c], R. Arróyave[a], I. Karaman[a,*]

[a] Department of Materials Science and Engineering, Texas A&M University, College Station, TX 77843, USA
[b] X-ray Science Division, Advanced Photon Source, Argonne National Laboratory, Lemont, IL 60439, USA
[c] Siberian Physical and Technical Institute, Tomsk State University, 634050 Tomsk, Russia

ARTICLE INFO

Article history:
Received 17 July 2020
Revised 23 December 2020
Accepted 28 December 2020
Available online 31 December 2020

Keywords:
Magnetic shape memory alloys
Martensitic transformation
Curie temperature
Crystallographic ordering
Microstructural size effects

ABSTRACT

In the present work, the effects of composition and heat treatments and the resulting microstructural changes on the martensitic transformation and ferromagnetic transition have been investigated in NiCoMnIn metamagnetic shape memory alloys. In this shape memory alloy system, it is observed that upon heat treatments at a wide temperature range, the onset temperature of the martensitic transformation follows a non-monotonic behavior with respect to heat treatment time, and the nature of the non-monotonic behavior is also a function of composition. This behavior cannot be attributed to well-known factors such as precipitation, change in local composition due to the precipitation and/or global degree of order. In this work, a systematic investigation through synthesis, thermal processing and characterization via thermo-physical measurements, transmission electron microscopy and in-situ synchrotron x-ray diffraction experiments has been used to correlate the non-monotonic dependence of the martensitic transformation and ferromagnetic transition temperatures to the evolution of $L2_1$ domains arising from a order/disorder phase transition. A thermodynamic model for the magneto-structural transition is combined with classical nucleation theory to further ascertain the role of microstructural length-scales on the onset of the martensitic transformation. This work thus provides understanding of the thermodynamic and kinetic factors that can be controlled to tune the coupled magneto-structural transformations in NiCoMnIn metamagnetic shape memory alloys.

1. Introduction

1.1. Overview

Shape Memory Alloys (SMAs) undergo displacive, diffusionless and reversible martensitic transformations (MTs). These reversible MTs mediate a wide variety of phenomena, ranging from the well-known shape memory and superelasticity effects [1–14] to the more recently discovered tunable thermal expansion [15–17] tunable stiffness [18,19], and giant elastocaloric effects [20–27]. Among SMAs, Metamagnetic Shape Memory Alloys (MMSMAs) [28–47] exhibit a large magnetization change across the MT due to the different magnetic ordering ––ferromagnetic (FM), paramagnetic (PM), anti-ferromagnetic (AFM)–– in the austenite (high temperature/symmetry) and martensite (low temperature/symmetry) phases, leading to strong interactions between configurational, thermal, structural and/or magnetic degrees of freedom [33,48,49]. These couplings enable an even wider range of complex phenomena, such as: magnetic field-induced transformation [50,51], magnetic exchange bias [52–54], magnetic shape memory effect [55–59], giant magnetocaloric effect (MCE) [60–73], linear change in magnetization with strain [74,75], magnetoresistance [76,77], strain-glass [49,78–82] and cluster spin-glass transitions [83–85].

Previous works have shown that it is feasible to modify the characteristics of the MT in MMSMAs in order to optimize their functional response. For example, one can modify the onset of the MT by altering its chemistry or the microstructure of the alloy, including constituent redistribution ––achieved through secondary thermal processing–– due to precipitation, phase-separation and/or configurational ordering. These microstructural modifications result in non-trivial changes to the MT temperature, the Curie tem-

* Corresponding author.
E-mail address: ikaraman@tamu.edu (I. Karaman).

https://doi.org/10.1016/j.actamat.2020.116616
1359-6454/

perature of the austenite, and the onset of the spin and strain glass temperatures in MMSMAs [47,49,86,87]. The extreme sensitivity of MMSMAs to minute alterations of its microstructure makes it possible for a single alloy composition to exhibit very different functional properties and behavior depending on its thermal history.

In many Heusler-based MMSMAs, the most common microstructure modification relies on the order-disorder (ODO) $L2_1$-B2 transformation. Originally, it was thought that the overall degree of order in the microstructure, controlled by the holding temperature during isothermal annealing experiments, was sufficient to explain the MT characteristics of these alloys as a function of process conditions [49]. Recently, however, we have come to realize that the dependence of the MT characteristics on thermal processing cannot be explained solely by changes in the overall $L2_1$ degree of order [46]. Specifically, it was found that the MT characteristics of $Ni_{45}Co_5Mn_{36.6}In_{13.4}$ MMSMAs do not vary monotonically with the heat treatment time at a given isothermal treatment temperature. Since the overall degree of order should increase monotonically with time, the non-monotonic nature of the MT response provided strong indication that more complex microstructural processes were in effect. To date, however, the nature of these microstructural degrees of freedom remains unresolved.

In this work, we aim to shed light on the question above by carrying a systematic experimental investigation aided by theoretical analysis. Previous work by the present group focused on single crystalline samples of a single composition and involved the examination of the effects of a few selected secondary heat treatments on the onset of the MT in $Ni_{45}Co_5Mn_{36.6}In_{13.4}$ alloys. While the earlier investigations revealed the impact of microstructural processes on the MT in this MMSMA system, the results were not sufficient to draw general conclusions and to properly deconvolute the observed relationship between microstructure and MT from other possible simultaneous effects, such as the ODO reaction mentioned above.

To address this, we have carried out an extensive investigation of the MT properties as a function of initial cooling rate, temperature and duration of heat treatments and composition using polycrystalline Mn-rich Co-doped Ni–Co–Mn–In MMSMAs of different Mn/In content. Thanks to the magneto-elastic interactions occurring during the MT in these alloys, the MT has an enhanced sensitivity to structural and microstructural changes, facilitating the investigation of the different contributions to the MT thermostability. Accordingly, the chosen chemistries and thermal processing widely modify the competition for phase stability between martensite and austenite, permitting us to examine the role of the different structural and microstructural factors on the onset of the MT.

Below, we introduce some basic background on Ni–Mn-based MMSMAs that will help understand the different correlations between structural and microstructural features and the characteristics of the MT. Some of these concepts are grouped/summarized in Fig. 1 following a typical processing-structure-properties diagram. In summary, the present study experimentally and/or theoretically demonstrates that: i) composition modifies the thermodynamics of the phase transformation through the modification of elastic and magnetic contributions to the free energies of the two competing phases; ii) secondary heat treatment (SecHT) temperature sets overall degree of order and rate of the microstructural change; iii) magnetic field and overall degree of order modifies the thermodynamic balance between austenite and martensite via magnetic contributions to the free energy differences between austenite and martensite; iv) SecHT duration determines the average length-scale of the microstructural features; v) initial HT cooling rate modifies the microstructure evolution path; and vi) microstructural features –Anti-Phase Boundaries (APBs) and $L2_1$ domain size– modify the onset of the transformation by producing barriers to the nucleation and/or propagation of martensite domains.

1.2. Effects of chemical composition on the metamagnetic behavior of magnetic shape memory alloys

Ni–Mn-based SMAs are off-stoichiometric Heusler-like alloys, with the $X_{50}Y_{50-X}Z_X$ compositions [88], where X and Y are transition metals, Ni and Mn respectively, and Z is a post-transition metal, Ga, In, Sn, Sb or Al [50,89,90]. In this three-sublattice system, low temperatures result in distinct occupation in all the sublattices leading to the so-called $L2_1$ ordered state. At higher temperatures, the occupation of two of the sublattices becomes indistinguishable, corresponding to the B2 configuration. The Ni–Mn-based SMAs can exhibit reversible martensitic transformations between body-centered cubic parent phases, which can present different long-range atomic order configurations, and body-centered tetragonal martensites, which can be non-modulated or modulated [91,92]. MT for the binary NiMn (Z=0) alloy occurs at a martensite start (M_S) temperature as high as 965 K [93]. On substituting Mn by Z atoms, MT temperatures decrease as a result of an increase in the lattice elastic constants, increasing the resistance against shear that is responsible for MT [94–96].

In addition to MT temperatures, the magnetic behavior of austenite and martensite also depends on Mn/Z content. Magnetism in Ni–Mn-based alloys has its origin on Ruderman-Kittel-Kasuya-Yosida (RKKY) exchange-type interactions. Following Buchelnikov *et al.* [97], the interaction between Mn–Mn pairs can be ferromagnetic or antiferromagnetic depending on the distance between neighboring Mn atoms: Nearest-Neighbor (NN) Mn-Mn pairs interact anti-ferromagnetically (AFM) while second NN Mn-Mn pairs interact ferromagnetically (FM). While at low temperatures austenite tends to be FM, the Z content greatly influences the onset of the MT and the austenite can be either in a ferromagnetic or paramagnetic state if the Curie temperature of austenite (T_C^A) lies below or above the MT temperature, respectively. When the cubic austenite transforms to the tetragonal martensite, the distance between the NN and second NN Mn-Mn pairs changes, and this tends to increase the number of Mn-Mn pairs with AFM interactions, counter-acting the strong FM interactions between Ni(Co)-Mn pairs. These interactions result in martensites with PM or weakly AFM magnetic order.

$Ni_{45}Co_5Mn_{50-X}In_X$ alloys with X around 13.3 transform around room temperature exhibiting FM→PM metamagnetic behavior with T_C^A around 380–400 K. In this system, the total entropy change during the MT can be approximated by the sum of the configurational, vibrational, magnetic and electronic contributions, $\Delta s_{tot} \approx \Delta s_{config} + \Delta s_{vib} + \Delta s_{mag} + \Delta s_{el}$ [98], and needs to be negative for the MT to occur. Because the MT is partitionless Δs_{config} is negligible. Δs_{vib} is negative as the austenite phase has considerably more entropy than the martensite due to anharmonic effects. Δs_{el} may be positive or negative depending on whether the electron concentration at the Fermi level increases or decreases during the transformation. Δs_{mag} is always positive because the system transforms from a magnetically ordered austenite to a disordered martensite.

Umetsu *et al.* [98] demonstrated a correlation between Δs_{mag} and the difference between FM transition and MT temperatures, T_C^A-M_S. Importantly, this strong dependence of Δs_{tot} on T_C^A-M_S via Δs_{mag} results in a measure that expresses the sensitivity of the phase stability to both intrinsic (e.g. composition) and extrinsic (e.g. external magnetic field) factors. For instance, an increase in In-content will stabilize the austenite, decreasing MT temperatures, increasing T_C^A-M_S difference, which further stabilizes the FM austenite. Another consequence of the dependence of the phase stability on Δs_{mag} is that the onset of the MT can be controlled through the application of an external magnetic field, according to the Claussius-Clapeyron relationship. In fact, a large-enough magnetic field can raise Δs_{mag} to the point that Δs_{tot} will be always

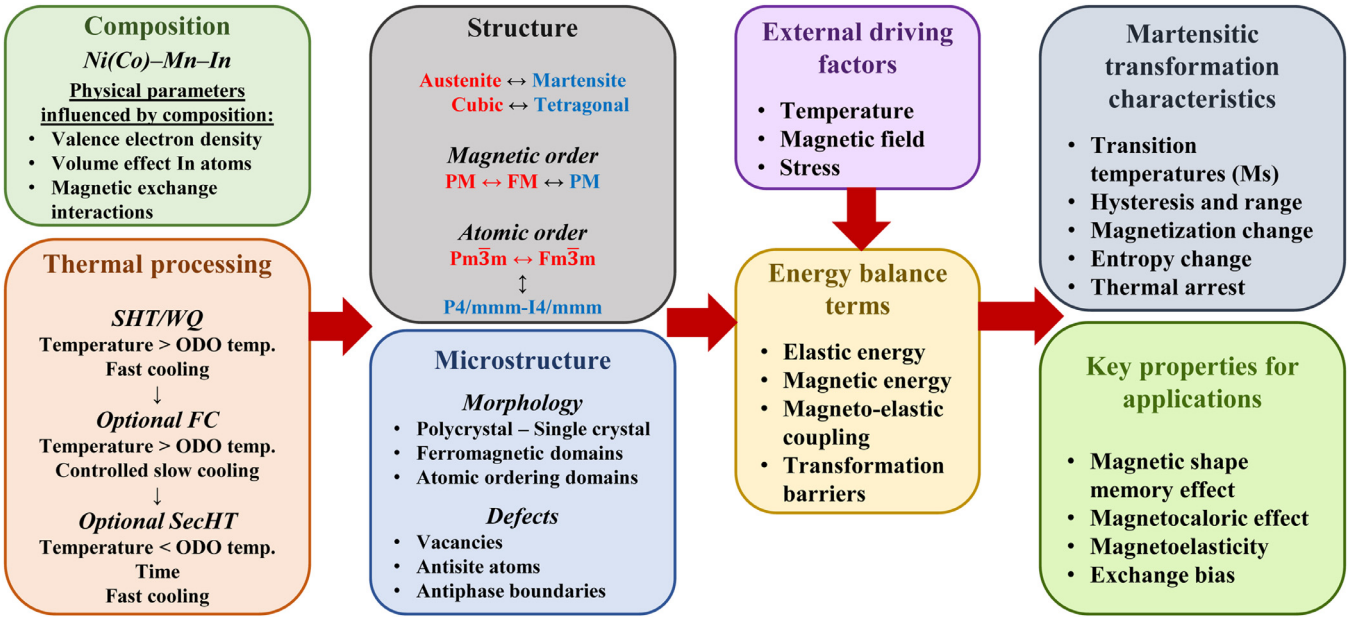

Figure 1. Processing-structure-property diagram for the present NiCoMnIn metamagnetic shape memory alloys depicting the influence of composition and thermal processing parameters on the martensitic transformation characteristics and other key properties, through their effect on the structural and microstructural configuration of the material and on the different energy contributions to the phase stability. Red/blue color relates properties in austenite/martensite. SHT: Solution Heat Treatment, WQ: Water Quenching, FC: Furnace Cooling, ODO: Order-Disorder, SecHT: Secondary Heat Treatment.

positive, and the MT will be completely suppressed [99]. Then, the austenite is said to be fully thermodynamically arrested.

1.3. Effects of Order-Disorder Transition on Martensitic Transformation characteristics

Ni–Co–Mn–Z Heusler-like alloys exhibit different degrees of configurational ordering depending on their composition and temperature [88]. The transition between these states is known as Order-Disorder (ODO) transition. $Ni_{45}Co_5Mn_{36.7}In_{13.3}$ alloys only show a single ordering transition between B2 and $L2_1$ phases at $T_{B2\text{-}L21}$ around 896 K [86]. Such $T_{B2\text{-}L21}$ is low enough to permit the quenching of high-temperature B2 order by fast cooling the material to room temperature, meaning that the final configurational order present at room temperature can be tuned [49,100]. Since the ODO requires atomic diffusion and investigated $Ni_{45}Co_5Mn_{50\text{-}X}In_X$ alloys transformed well below 373 K, there should be no overlap between ODO transition and MT. As consequence, martensite will have the same NN and second NN atomic species as austenite and thus will inherit austenite's degree of configurational order.

Many properties of the Ni–Co–Mn–In alloys and its MT transformation depend on the quenched-in disorder through the different characteristics of the B2 and $L2_1$ phases. In particular, the redistribution of Mn atoms through the crystal alters the strength of the FM and AFM interactions, resulting in higher T_C^A and magnetic moment for the high order $L2_1$ phase [47,86,101]. Consequently, the $L2_1$ degree of order affects the MT phase stability varying Δs_{mag} and, then, it modifies the MT temperatures following the relationship between Δs_{tot} and T_C^A-M_S range [87]. Notably, samples with different degree of order can present different martensitic structures: modulated BCT (6M) or non-modulated BCT (2M, $L1_0$) martensite for the ordered and disordered samples respectively [86].

The degree of order thus adds a degree of freedom for tuning the characteristics of the MT in $Ni_{45}Co_5Mn_{50\text{-}X}In_X$ alloys which can be adjusted through simple thermal treatments. Note that this tuning mechanism is only possible for the MMSMAs in which disorder can be quenched-in during the thermal process. Sn and Sb alloys present a more stable $L2_1$ phase than In and Ga alloys [102], so their M_S and T_C temperatures are mostly unaffected by heat treatments. In addition, the strong dependence of the MT thermostability on Δs_{mag} of In alloys make them more sensitive to order changes than other ferromagnetic SMAs, like Ni–Ga–Fe [103] and Ni–Mn–Ga [104].

1.4. Effects of microstructure on Martensitic Transformation characteristics

A recent investigation by Bruno *et al.* [46] has shown that the properties of the MT in Ni–Co–Mn–In alloys evolve during secondary annealing treatments for long periods of time when the samples are annealed below 773 K. Such evolution spans time scales longer than typical secondary heat treatments performed in previous works [49]. Bruno *et al.* showed that M_S could present a minimum when the alloy was annealed at 773 K: M_S decreased between the initial SHT condition and 0.25 h of secondary heat treatment (SecHT), from 260 to 236 K, but it increased back when the material was annealed for 0.5 and 3 h, to 270 and 297 K, respectively. Such behavior could not be explained only with the monotonic evolution of the overall degree of order and Bruno *et al.* proposed the competition between the ODO process and the annihilation of quenched-in vacancies as a possible explanation for this behavior.

Recent results from both experiments and *ab initio* calculations [105], however, have indicated that the atomic ordering and the quenched-in vacancy annihilation processes in Ni–Co–Mn–In alloys are much quicker than the time-evolution of the MT temperatures during secondary thermal processes. It is therefore unclear what the nature of the microstructural feature(s) affecting the thermostability of the MT is. In order to be able to discern the nature of the source of the observed SecHT duration-dependence, it is necessary to carry out an extensive investigation looking for all the implications of the microstructural dependence on the MT properties.

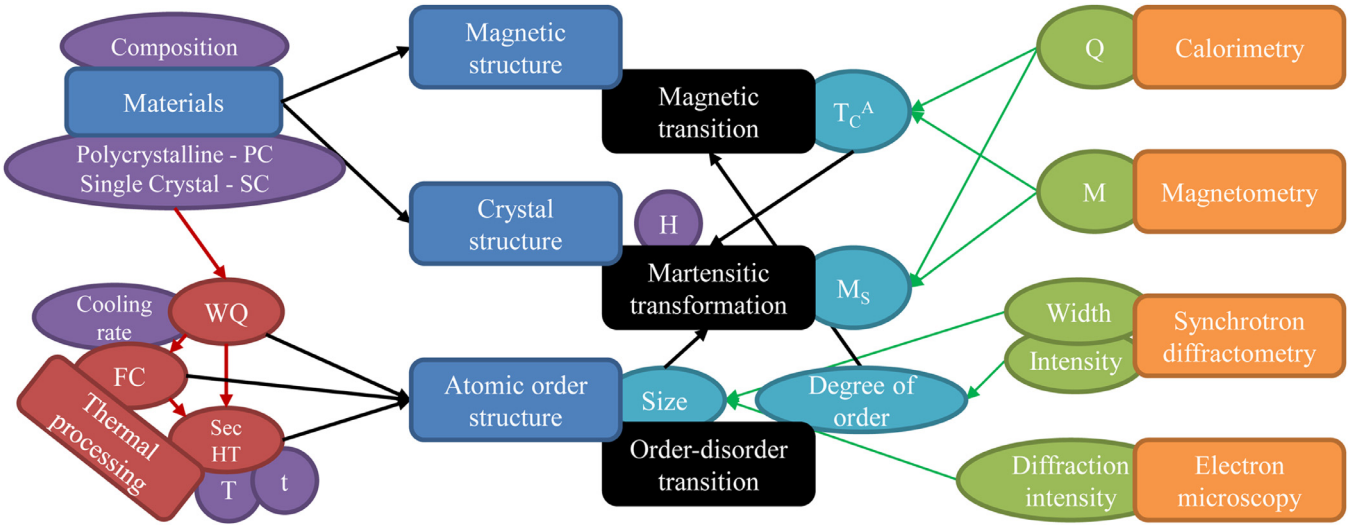

Figure 2. Experimental flowchart depicting the different heat treatment paths (red), the experimental techniques (orange) and the studied transitions (black). Main experimental variables (purple): Mn/In composition, polycrystalline PC, single crystal SC, heat treatment cooling rate, secondary heat treatment T temperature and t time, and H magnetic field. Measured variables for characterization (green): Q heat exchange, M magnetization, width and intensity of diffraction peaks and dark field diffraction intensity. Transition characteristic properties (teal): T_C^A Curie temperature of the austenite, M_S martensitic transformation onset temperature, $L2_1$ degree of order and average $L2_1$ domain size. Red arrows: material processing paths before characterization. Green arrows: characterization. Black arrows: dependencies/relationships.

1.5. The present work

The objective of the present work is to investigate the dependence of the MT characteristics in Ni-Co-Mn-In MMSMAs with different In contents on the evolution of the material microstructure occurring during thermal treatments. First, we introduce the experimental procedure utilized to characterize the martensitic transformation, the ferromagnetic transition in the austenite and the microstructure of the material. We then examine the dependence of the M_S temperature on composition, applied magnetic field, and thermal processing parameters. These changes are then correlated to the Curie temperature of the austenite as well as the overall degree of $L2_1$ ordering. Next, we attempt to elucidate the mechanisms responsible for the non-monotonic response in the MT by connecting classical nucleation theory with the time evolution of microstructural length-scales associated with the evolution of $L2_1$ domains. Finally, we demonstrate the apparent correlation between the evolution of MT temperatures and the observed microstructural length-scales between a precipitation-hardened non-magnetic SMA and the present Ni-Co-Mn-In MMSMAs which does not feature precipitation hardening.

2. Experimental procedures

Polycrystalline alloys with the nominal compositions of $Ni_{45}Co_5Mn_{50-X}In_X$ at.%, X ranging from 13.3 to 13.7 were vacuum induction melted using high purity constituents. Single crystal ingots of $Ni_{45}Co_5Mn_{36.6}In_{13.4}$ were grown via the Bridgman method under a He environment. Figure 2 schematically summarizes all thermal processing procedures and experimental studies performed in the present work. Initially, relatively large polycrystalline plates (about $40 \times 5 \times 1$ mm^3) were cut and homogenized at 1173 K for 24 hours and Water Quenched (WQ). After this initial Solution Heat Treatment (SHT), the bars were cut into smaller samples (about $5 \times 1 \times 1$ mm^3). Then, the samples were exposed to different thermal processing paths, as shown in Fig. 2. A fraction of the samples was heat-treated again at 1173 K for 1 h and slow cooled (furnace cooling - FC) to 300 K inside the furnace with a controlled cooling rate of 0.55 K/min.

Most WQ and FC samples were, in addition, secondary heat-treated (SecHT) at different temperatures between 573 K and 873 K for periods of time ranging from 0.25 h to 240 h. Then, the samples were water-quenched in order to freeze the degree of $L2_1$ order achieved at different isothermal treatment temperatures. Selected SecHTs resulted in a large variety of microstructures, with different degrees of $L2_1$ crystallographic ordering, and a variety of domains sizes and morphologies. Note that during each of the heat treatments, the material was sealed in a quartz tube under a protective low-pressure high-purity Ar atmosphere to minimize oxidation. Having a large number of heat treatment conditions, we would like to direct the reader to the sample nomenclature and description in Table 1.

The temperature dependence of the DC magnetization under constant applied magnetic field of 0.05 T, 1 T or 7 T was measured using a Quantum Design MPMS SQUID VSM magnetometer. Thermomagnetic measurements were made during cooling–heating cycles between 10 K and 400 K at 5 K.min^{-1}. Fig. 3a shows the magnetization response during a cooling-heating cycle for two different samples in the temperature range of the MT. The transformation is revealed by the magnetization difference between the FM austenite and the weak-magnetic martensite, and the hysteresis between the forward and reverse transformations. Characteristic MT temperatures, M_S, martensite finish (M_F), austenite start (A_S) and austenite finish (A_F), were obtained from the magnetization change across the transformation. The MT temperatures were determined using the area between the transformation peak of the temperature derivative of the magnetization and the baseline obtained from the temperature dependence of the magnetization outside the MT range, as shown in Fig. 3b. MT temperatures correspond to the temperature at which there has been a 5% (95%) of the forward (reverse) transformation magnetization change. This method is superior to the typical tangent-based method in cases in which the MTs are diffuse or incomplete [106,107].

The temperature dependence of the calorimetric response was measured in a TA Instruments DSC Q2000 with cooling/heating rates of 10 K.min^{-1}, over a temperature range (170–420 K) spanning both the magnetic and, in some cases, the martensitic transformations. Figure 4 presents an example of the calorimetric response and its temperature derivative for a polycrystalline (PC)

Table 1
Description of the nomenclature used to describe the composition and processing of the NiCoMnIn samples used in this study.

Nomenclature	Description
PC	Polycrystalline
SC	Single crystalline
InX	$Ni_{45}Co_5Mn_{50-X}In_X$ atomic%
SHT/WQ	Solution heat treatment / Water Quenched 24 hrs. at 1173 K
FC	Furnace Cooled SHT/WQ + 1 hr at 1173 K and controlled slow cooling (0.55 K/min)
SecHT	Secondary Heat Treatment, XKYh Either WQ or FC + Y hrs at X K, Water quenched

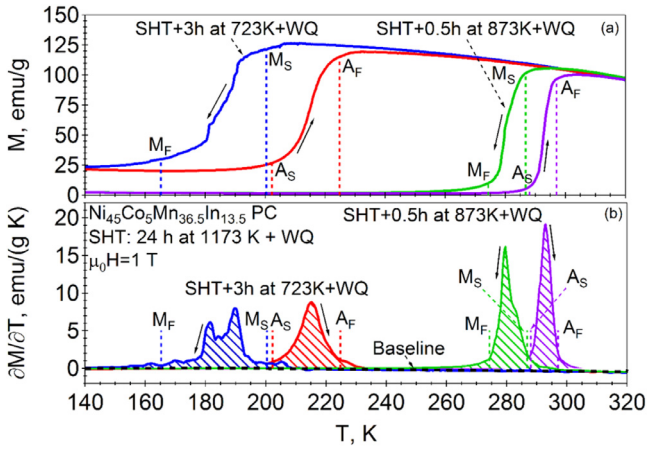

Figure 3. (a) Temperature dependence of the magnetization and (b) of the temperature derivative of the magnetization for two polycrystalline (PC) $Ni_{45}Co_5Mn_{36.5}In_{13.5}$ MMSMAs with the same solution heat treatment, 1173 K for 24 hr and water quenched (WQ), but different secondary heat treatments: 3 h at 723 K+WQ (cooling in blue, heating in red) and 0.5 h at 873 K+WQ (cooling in green, heating in purple). The positions of the MT characteristic temperatures M_S, M_F, A_S and A_F are indicated by vertical dashed lines. In (b), for simplicity, only the baseline of the 3 h at 723 K+WQ peak is shown. The area below the temperature derivative of the magnetization curves, used for the calculation of the MT temperatures is mark with a diagonal pattern.

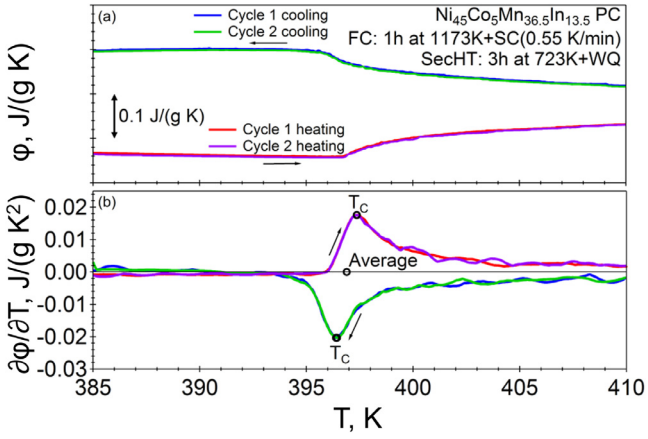

Figure 4. (a) Temperature dependence of the calorimetric response, normalized by sample mass and temperature rate, and (b) of its temperature derivative during two thermocycles for a polycrystalline (PC) $Ni_{45}Co_5Mn_{36.5}In_{13.5}$ MMSMA, controlled slow cooled (SC) at 0.55 K/min from 1173 K to room temperature (furnace cooled – FC) and secondary heat treated (SecHT) at 723 K for 3 h followed by water quenching. The figures show a close up around the Curie temperature of the austenite. Arrows indicate the direction, cooling/heating, of the temperature cycle. Open circles in (b) indicate the peak temperatures from which the Curie temperature was calculated as an average of the four curves (displayed in the middle).

In13.5, FC, 723K3h SecHT sample close to the FM transition. The magnetic transition produces a non-linear change on the calorimetric response of the material because of the change in heat capacity [108], as shown in Fig. 4a. This peak can be used to determine T_C^A. To reduce the uncertainty in the determination of the Curie temperature, T_C^A was calculated as the average of the peak temperatures for four different temperature ramps, two on cooling and two on heating, for each sample.

Transmission X-Ray Diffraction experiments were conducted at the Advanced Photon Source, Argonne National Laboratory using high-energy synchrotron radiation. Different experimental procedures were carried out on single crystalline (SC) In13.4 and PC In13.3 samples with either WQ or FC thermal protocols, sometimes followed by SecHT during the in-situ high energy synchrotron experiments. Polar diffraction spectra for these samples were obtained at 423 K (to ensure the material was well above M_S). All samples displayed diffracted intensities corresponding to the planes (hkl) with h+k+l = even number, which indicates B2+$L2_1$ phases, and with h+k+l = odd number, produced only by $L2_1$ domains [102,109,110]. Examples of the diffraction spectra for SC In13.4 WQ and FC samples are shown in Figs. 5a and 5b, respectively. In order to mimic the evolution of the microstructure during conventional heat treatments, SC and PC samples with only initial heat treatment (WQ or FC) were heated at 25 K/min from room temperature to different temperatures below the ODO transition temperature, and then held isothermally. During this process, polar diffraction patterns were recorded in regular time-intervals. The intensity of the (111) diffraction spots was integrated as a func-

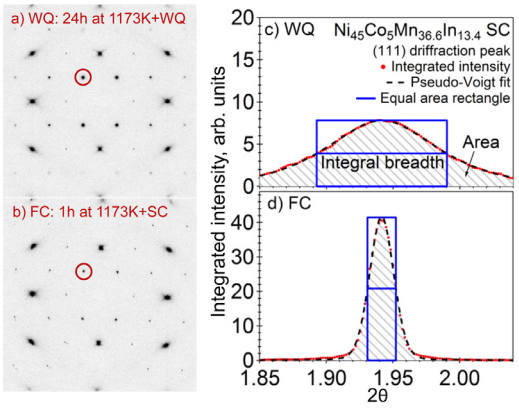

Figure 5. Polar synchrotron transmission x-ray diffraction spectra for two single crystalline $Ni_{45}Co_5Mn_{36.6}In_{13.4}$ samples with (a) WQ (24 h at 1173 K + water quenched) and (b) FC (WQ + 1 h at 1173 K + slow cooled (SC) (0.55 K/min) thermal processing conditions, obtained in austenite (423 K). One of the (111) diffraction spots is marked with open red circle in both spectra. The integrated intensity corresponding to (111) diffracting planes as a function of Bragg angle for the same (c) WQ and (d) FC samples. Experimental data (red dots) is compared with Pseudo-Voigt profile fitting (black dashed line) and a rectangle with equal area and height of the fitting curve (blue solid line). The peak area (diagonal pattern, dependent on $L2_1$ phase fraction) and peak broadening (integral breadth, dependent on crystallite size and instrumental broadening, blue line) are shown. Note the different y-axis of (c) and (d).

tion of the Bragg angle and utilized to track the evolution of the $L2_1$ phase characteristics. As shown in Figs. 5c and 5d, the (111) diffraction peaks were fit using a Pseudo-Voigt profile.

The change in the degree of order was estimated from the evolution of the square root of the peak area. In addition, the average size of the coherently diffracting domains was calculated using the Scherrer equation $L=K\lambda / B\cos\theta$ [111,112]; where λ is the wavelength of the synchrotron radiation (0.1173 Å), B is the integral breadth of the Pseudo-Voigt peak (after being corrected for instrument broadening), K is a factor depending on the shape and orientation of the diffracting domains, which is 1.1547 for cubic-like crystallites for the (111) peak [113], and θ is the Bragg angle. In the present case, the coherently diffracting domains for the (111) diffraction peak are the $L2_1$ ordered domains and the average size L will correspond to the typical length scale of the $L2_1$ domains perpendicular to the (111) diffraction plane.

The $L2_1$ domain microstructure of SC In13.4 samples was studied with a FEI Tecnai G2 transmission electron microscope using dark field imaging mode using the (111) diffraction peak of the cubic austenite. Different single crystalline samples were subjected to solution heat treatment and water quenching (WQ), WQ and secondary heat treatment (SecHT) at 673K for 3 h, and WQ + SecHT at 673K for 24h thermal treatments. Then, TEM foils of 100 μm thickness and 3 mm diameter were prepared with their surface normal oriented along the [011] austenite direction. These foils were twin-jet electropolished using a 1:3 nitric acid to methanol electrolyte under 20 V at 243 K.

To compare the effects of microstructural length scales on the MT characteristics in another alloy system with nanoprecipitates as the feature controlling the length scale, polycrystalline $Ni_{50.3}Ti_{34.7}Hf_{15}$ at.% shape memory alloy was prepared using vacuum induction melting of elemental Ni, Ti and Hf (99.98%, 99.95% and 99.9% purity, respectively). The material was homogenized under vacuum at 1323 K for 72 h and furnace cooled to room temperature. Then, the homogenized ingot was sealed in a mild steel can and hot extruded at 1173 K with an area reduction of 7:1. Samples of 1 mm thickness and 5 mm diameter were cut and solution heat treated at 1173 K for 1 h to dissolve any possible secondary phases formed during fabrication, followed by systematic SecHTs performed at 723, 773 or 823 K for 1, 3, 10, 24 and 48 hours, and water quenching. This procedure created a set of samples with different precipitate sizes and volume fractions for modifying the MT characteristics as explained in detail in [114].

3. Experimental Results

Figure 6 presents the dependence of M_S on both temperature and duration of the SecHT for PC (In13.3, In13.5, In13.6, In13.7) WQ samples as determined from their thermomagnetic responses. Note that each point corresponds to a single sample that has been treated either with only the initial SHT, or with the SHT plus a SecHT. Some of the main trends can be summarized by focusing on the results in Fig. 6a, which correspond to the data for the In13.3 samples. The M_S of the samples heat treated at 723K first decreases from 275.5 K (SHT sample) to 233.7 K (0.5h sample) and then increases significantly to 301.4 K after 24 h of SecHT. Further evolution of M_S becomes less sensitive to longer heat treatment times. The curves for the 773K, 673K and 573K samples, in Fig. 6a, exhibit similar trends as the 723K curve, but with three key differences. First, the M_S increases with heat treatment temperature for samples with same SecHT duration. Second, the exposure time required to achieve the minimum in M_S temperature increases on decreasing annealing temperature. Third, the drop in M_S between the initial SHT state and the minimum increases on decreasing SecHT temperature, reaching a difference of about 125 K for the 573K curve.

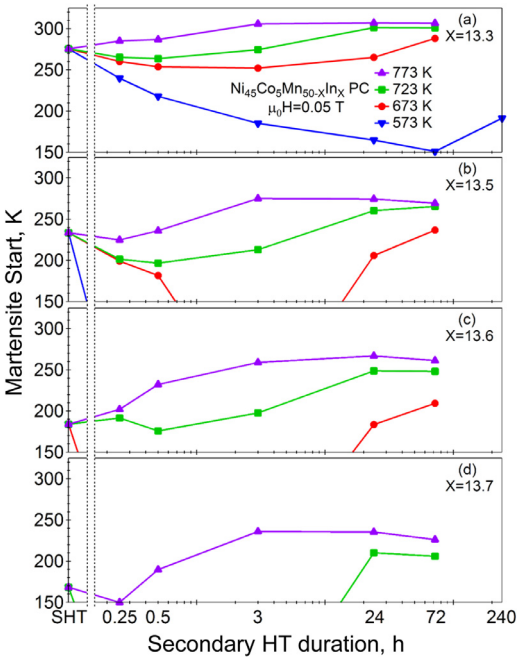

Figure 6. Martensite start temperature after solution heat treatment (SHT) at 1173 K for 24 h and water quenching (WQ), followed by secondary heat treatments of different duration and temperature, 573 K (blue reverse triangles), 673 K (red circles), 723 K (green squares) and 773 K (purple triangles) for $Ni_{45}Co_5Mn_{50-X}In_X$ MMSMAs with (a) X=13.3, (b) X=13.5, (c) X=13.6 and (d) X=13.7 at.%. M_S falling below the bottom axis indicates that the sample did not show MT (transformation arrest). SecHT duration axis is in logarithmic scale.

These general trends were reproduced in the alloys with higher In-contents, as shown in Figs. 6b-d. These figures demonstrates that substituting Mn by In atoms results in a decrease in M_S, in agreement with previous results [92,115]. Interestingly, in some cases the increase in In-content leads to the full arrest of the MT [116]. Note that for all cases presented in Fig. 6, no sample underwent a MT with M_S below 150 K. While all compositions followed the same trends observed for In13.3, when the expected M_S temperature was below a certain limit, close to 150 K for $Ni_{45}Co_5Mn_{50-X}In_X$ alloys, the transformation became arrested. The origin of the thermodynamic arrest is due to the competition between the magnetic and vibrational contributions to the MT entropy change, as the vibrational contribution significantly decreases on cooling below 150 K in these alloys [99].

Figure 7 displays the dependence of the M_S temperature on SecHT conditions for the PC In13.3 WQ samples during thermal cycles under different applied magnetic fields: 0.05 T, 1 T and 7 T. As can be seen for the 773K samples, Fig. 7a, the increase of the applied magnetic field stabilizes the ferromagnetic austenite, which decreases the M_S temperature [98]. The same is true for the 723K samples in Fig. 7b, with the change in M_S between 1 T and 7 T curves being larger for the 723K samples than for the 773K ones. This effect is caused by the decrease of the MT entropy change: the 723K samples transformed at lower temperatures, increasing the T_C^A-M_S difference, which enhances the magnetic ordering, and thus the stability, of the austenite. On the other hand, samples transforming at lower temperatures tend to show a lower MT entropy change and––as predicted by the Clausius-Clapeyron relationship––are more sensitive to the application of a magnetic field. In the limit, the applied magnetic field can stabilize the austenite enough to induce the magnetic-field arrest of the MT, as can be observed in Figs. 7c and 7d.

It is important here to compare 673K curves in Fig. 7c under different magnetic fields with the 673K results under 0.05T for dif-

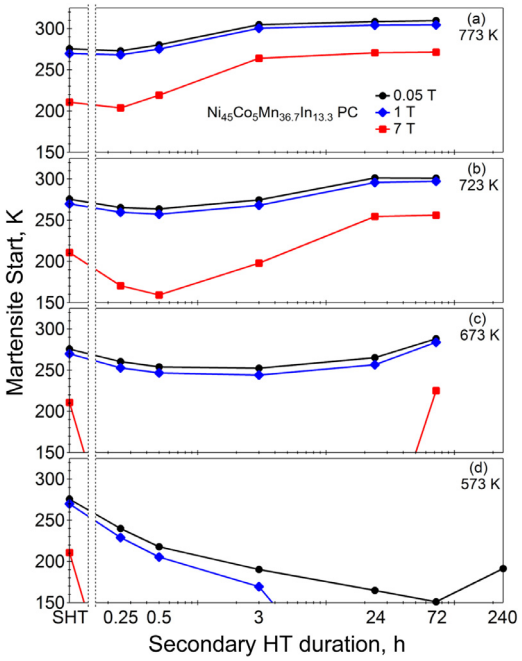

Figure 7. Martensite start temperature after solution heat treatment (SHT) at 1173 K for 24 h and water quenching (WQ), followed by secondary heat treatments of different duration and temperature, (a) 773 K, (b) 723 K, (c) 673 K and (d) 573 K for $Ni_{45}Co_5Mn_{36.7}In_{13.3}$ MMSMAs. M_S is shown for cooling-heating thermal cycles under different constant applied magnetic fields: 0.05 T (black circles), 1 T (blue diamonds) and 7 T (red squares). SecHT duration axis is in logarithmic scale.

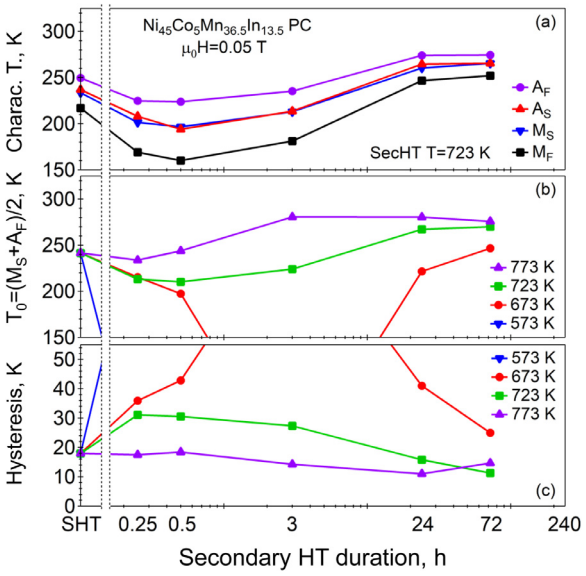

Figure 8. (a) Characteristic martensitic transformation temperatures, M_S (blue reverse triangles) M_F (black squares) A_S (red triangles) and A_F (purple circles), after SHT, followed by SecHT at 723 K for different durations. (b) Critical temperature $T_0=(M_S+A_F)/2$ and (c) thermal hysteresis ($(A_F+A_S-M_S-M_F)/2$) after SHT and SecHTs of different temperatures and durations, 573 K (blue reverse triangles), 673 K (red circles), 723 K (green squares) and 773 K (purple triangles). All cases for $Ni_{45}Co_5Mn_{36.5}In_{13.5}$ samples under magnetic field of μ_0H=0.05 T. SecHT duration axis is in logarithmic scale.

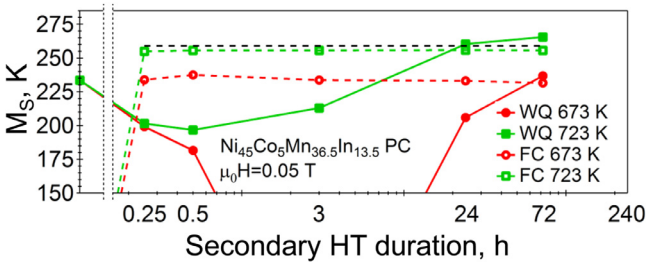

Figure 9. Martensite Start temperature of $Ni_{45}Co_5Mn_{36.5}In_{13.5}$ samples which initial homogenization heat treatment had different cooling rates: uncontrolled fast cooling (Water Quenching, full symbols, solid lines) and controlled slow cooling (Furnace Cooling, open symbols, dashed lines); following by secondary heat treatments of different duration performed at 673 K (circles) or at 773 K (squares). Color lines are guides for the eye connecting the points. Black dashed horizontal line is a constant temperature (perfectly flat) line for easy comparison with the SecHT duration-independence of M_S for FC samples. SecHT duration axis is in logarithmic scale.

ferent compositions (In13.3, In13.5, In13.6) in Fig. 6 (red circles). This comparison demonstrates that there is an equivalence in modifying the phase stability with the application of a magnetic field and through small changes in composition. Such similarity arises from the fact that these alterations will, directly or indirectly, have a significant impact on the magnetic contribution to the free energy difference between the different phases.

Note that curves in Figs. 6 and 7 are grouped by composition and SecHT temperature, respectively. If Fig. 7 were grouped by intensity of applied magnetic field, it would show a pattern very similar to the one observed in Fig. 6. However, grouping the curves by SecHT temperature helps visualizing the trends for the location (in time) for the minimum in M_S at different SecHT temperatures. In this way, Figs. 6 and 7 demonstrate that the SecHT time required to achieve the M_S minimum does not have a significant dependence on composition or applied magnetic field. From these results, it is apparent that the time required to achieve M_S minimum only depends on the SecHT temperature.

In general, the observations for M_S temperature reported above are also valid for the other characteristic temperatures of MT: M_F, A_S and A_F. As an example, Fig. 8a presents the evolution of all four characteristic MT temperatures for PC In13.5 WQ samples that were secondary heat treated at 723 K. Notably, the same is true for the average of M_S and A_F temperatures, which is often considered as the critical temperature, T_0, at which austenite and martensite phases are at thermodynamic equilibrium. This similarity can be clearly seen by comparing the dependence of M_S and calculated T_0 temperatures on the SecHT temperature and duration for PC In13.5 WQ samples in Figs. 6b and 8b, respectively. It is important to note here that the changes in M_S (and T_0) temperature can also be correlated with the variation of other important characteristics of the transformation, such as thermal hysteresis and MT driving force. Fig. 8c presents the dependence of thermal hysteresis, defined here as $(A_F+A_S-M_S-M_F)/2$, on the SecHT temperature and duration for PC In13.5 WQ samples. If we compare this figure with the evolution of M_S and T_0 on Figs. 6b and 8b there is a clear inverse correlation between the evolution of the transformation temperatures and the thermal hysteresis. Note that the thermal hysteresis is assumed to approach infinity in Fig. 8c for the 673K 3h and all 573K samples, for which the MT is fully suppressed, as thermal hysteresis continuously increases while approaching the arrest conditions.

The dependence of the MT on temperature and time of the SecHTs was also investigated for the furnace cooled (FC) samples. WQ and FC samples differ on the initial microstructural state of the material prior to the SecHT procedures due to their different initial cooling rate. Note that the samples were always water-quenched to complete the secondary heat treatments. Figure 9 displays a comparison between M_S temperature of PC In13.5 (both WQ and FC) samples after exposing them to SecHT at 673 K or 723 K for different amounts of time. In the present work, PC In13.3 FC sample (no SecHT) did exhibit an MT with M_S at 241 K, while PC (In13.5, In13.6, In13.7) FC samples did not experience any MT (MT is fully arrested). The fact that PC In13.5 FC sample did not transform to

martensite is clearly indicated in Fig. 9 as FC 673K and FC 723K curves starting below the bottom axis.

Fig. 9 demonstrates that the response of the WQ and FC samples to SecHTs is notably different. The WQ 673K and WQ 723K curves (solid lines) follow a non-monotonic behavior, with M_S minima at 0.5 h for WQ 723K and 3 h for WQ 673 K (fully arrested sample). In contrast, FC 673K and FC 773K curves had a large shift in M_S between the initial state (fully arrested) and samples secondary heat treated for 0.25 h, raising M_S to 234 K and 255 K, respectively, and became SecHT time-independent beyond this point, presenting no M_S minimum. The WQ and FC curves seem to converge for long SecHTs, with the time necessary to achieve this convergence being a strong function of temperature: 72 h for 673 K, 24 h for 723 K and 3 h for 773 K (last case not shown in Fig. 9 for brevity). Finally, the main similarity between the WQ and FC samples is that M_S for 723K samples is higher than M_S for 673K ones, likely due to a lower overall degree of order in 723K samples.

4. Discussion of the Results

The main objective of the discussion section is to better examine how the structure and microstructure of the materials is evolving during the thermal procedures applied here and correlate such evolution with the observed behavior of the MT characteristics.

4.1. The evolution of the degree of $L2_1$ order

The unexpected non-monotonic behavior observed in Figs. 6 to 9 seems to be a result of one or more processes occurring in the material during the thermal treatments. The B2-$L2_1$ order-disorder transition is a second order phase transformation that requires thermally activated atomic diffusion, so its product microstructure depends both on temperature and time. It is thus natural to assume that this process may be responsible for the observed non-monotonic evolution of M_S, and thus, of the MT characteristics. Previously, Bruno *et al.* [46] suggested that during the first stage of the M_S evolution, between the SHT state and M_S minimum, the behavior of the MT temperatures could be dominated by the change in overall degree of $L2_1$ order: a continuous increase of the degree of order would decrease MT temperatures. Under this assumption, the subsequent evolution of M_S would be dominated by a long-term change in the microstructure, which was suggested to be connected to the annihilation of vacancies. Such kind of long-term evolution of the overall degree of order has been observed before in Ni-Mn-based alloys. For example, Seguí and Cesari [117] observed the evolution of the MT temperatures and Curie temperature in a Ni(Co)-Mn-Ga alloy for more than 10^4 min when the material was heat treated at 470 K. In such experiments, though, the evolution of the MT temperatures was monotonic with heat treatment time (and implicitly with the change of order).

Experiments were, thus, carried out here to determine whether or not the time-scale of evolution of the degree of order is comparable to the time-scale of the change in M_S observed in Fig. 6. Figure 10 shows the time evolution of the square root of the intensity of the $(111)_{L21}$ diffraction peak, normalized with the intensity of the solution heat treated sample at low temperature, recorded during the high-energy transmission XRD experiments in SC In13.4 WQ samples in-situ heat treated to 680 K, 745 K and 790 K. This figure represents the evolution of the $L2_1$ order parameter during both heating and isothermal stages. Note that $t = 0$ min was chosen so the samples has the same temperature during the heating stage. The samples achieve target isothermal temperature at different times, as indicated by the vertical dashed lines.

At time $t = 0$ min, all the samples had a significant amount of quenched-in disorder as they had been water-quenched. At low temperatures, the quenched-in disordered state would be

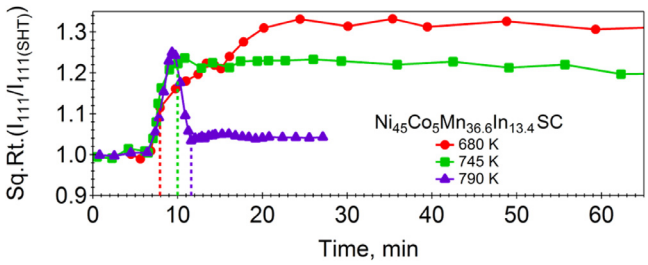

Figure 10. Square root of the normalized intensity of the $(111)_{L21}$ diffraction peak for a single crystalline $Ni_{45}Co_5Mn_{36.6}In_{13.4}$ MMSMA during the in-situ heat treatments at 680 K (red circles), 745 K (green squares) and 790 K (purple triangles), recorded using the high energy transmission XRD (synchrotron) experiments. Color vertical dashed lines indicate the transition between the heating and isothermal stages.

metastable and there would be a thermodynamic driving force for ordering. However, at temperatures below 573 K no evolution towards ordering was observed due to sluggish atomic diffusion. Further increase in temperature increased the atomic mobility and the samples' degree of order started to evolve towards equilibrium. We note that the change in degree of order may not be monotonic since a sample that is initially disordered may first evolve towards a more ordered state as it reaches intermediate temperatures but it then can devolve back towards a more disordered state if the temperature increases further. This can be observed in the sample heated to 790 K which reached its maximum degree of order at about 750 K, only to disorder further on increasing temperature. In contrast, the 680 K sample exhibited a near-monotonic increase in the degree order as a function of time as it progresses towards a more ordered state.

Regardless of the specific time evolution of the degree of order, the significance of these experiments is that, in all cases, the samples reached their equilibrium state within 0.5 h. In comparison, Fig. 6 shows that M_S minimum occurs after heat treatments of 3 h (0.5 h) for 673K (723K) samples. This suggests that time required to reach a stable overall degree of order is notably shorter than the time-scale of the evolution of MT temperatures. In other words, overall degree of $L2_1$ order must be stable much before the M_S reaches its minimum level in Fig. 6.

Further indirect information on the evolution of atomic order during SecHT can be obtained from the evolution of the Curie temperature of the austenite, T_C^A, of the post-heat treated (final state) samples since $L2_1$ phase presents an enhanced magnetic moment as compared to B2 phase. As a consequence, a sample with quenched-in disorder is expected to present a lower Curie point than a more ordered sample. The Curie temperatures were measured for the same final state samples used for characterizing MT characteristics, Figs. 6 to 9, so direct comparison between the evolution of T_C^A and M_S temperatures can be established. Figure 11 shows the dependence of T_C^A on both temperature and duration of the SecHT for PC (In13.3, In13.5, In13.7) WQ samples as determined from the calorimetric response.

To begin with, a significant change in T_C^A occurs between SHT samples and the 0.25h samples. This T_C^A shift is bigger on decreasing annealing temperature, with the exception of two cases where samples annealed at 673 K presented similar or higher T_C^A than the correspondent isochronal 573K samples. We suggest that this initial T_C^A shift between the SHT and 0.25h samples results from the change in overall degree of order observed in Fig. 10. In this case, the initial T_C^A shift should be proportional to the $L2_1$ ordering difference between the SHT state and the thermal equilibrium degree of order at SecHT temperature, where the two observed exceptions may be due to slow kinetics at 573 K. Beyond the initial T_C^A shift, a further change in T_C^A can be observed on increas-

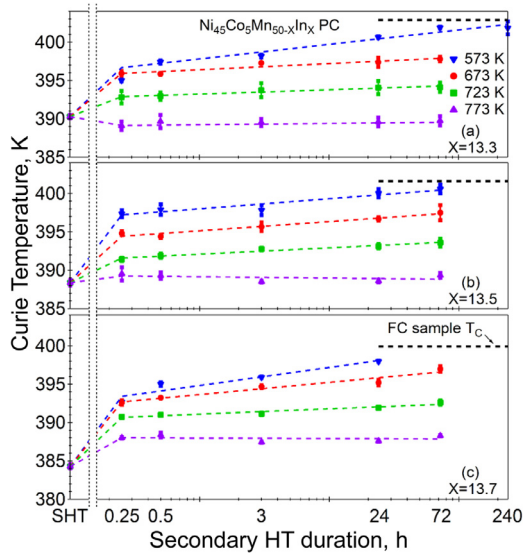

Figure 11. Curie temperature of the austenite after solution heat treatment (SHT) at 1173 K for 24 h, followed by secondary heat treatments of different duration and temperature, 573 K (blue reverse triangles), 673 K (red circles), 723 K (green squares) and 773 K (purple triangles) for $Ni_{45}Co_5Mn_{50-X}In_X$ MMSMAs with (a) X=13.3, (b) X=13.5 and (c) X=13.7 at.%. Dashed color lines are just guides for the eyes. Black dashed horizontal lines represent the Curie temperature for a sample slow cooled (furnace cooled – FC) at a rate of 0.55 K/min. Error bars represent the standard deviations after averaging the measured Curie temperatures for the different cooling and heating runs, see Fig. 3.

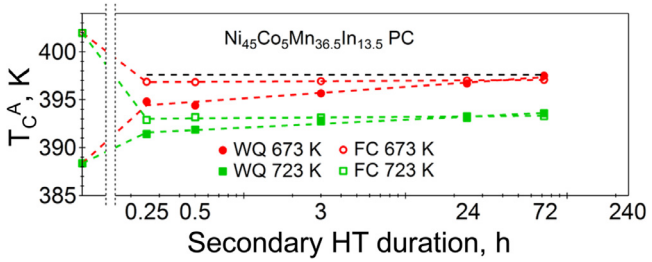

Figure 12. The evolution of the Curie temperature of the austenite phase (T_C^A) in $Ni_{45}Co_5Mn_{36.5}In_{13.5}$ samples, which had different cooling rates after the initial solution heat treatment: uncontrolled fast cooling (Water Quenching - WQ, full symbols) and controlled slow cooling (Furnace Cooling – FC, open symbols); followed by secondary heat treatments of different duration performed at 673 K (circles) or at 723 K (squares). Dashed color lines present are guides for the eyes. Black dashed horizontal line is a constant temperature (perfectly flat) line for easy comparison with the SecHT duration-independence of T_C^A for the FC samples. Error bars are not shown for visual clearness: average error was ±0.3 K (1σ), well below the magnitude of the differences between WQ and FC curves.

ing annealing time, at a rate that is much slower than the initial change from a relatively disordered state (SHT) to a more ordered one (SecHT). The trends suggest that the Curie temperature evolves in logarithmic time, although data density is low and scattering is significant.

Figure 12 presents the effects of SecHTs on T_C^A of the PC In13.5 samples with two different initial structural states achieved via controlling the cooling condition after solution heat treatment: water quenched (WQ) and controlled slow cooled (furnace cooled – FC). SecHTs were performed at 673 K and 723 K. Note that data for WQ samples also appears in Fig. 11b. During the slow cooling process of the FC samples, the material has plenty of time for the ordering process to occur. Then, FC samples present high overall degree of order and Curie temperature. Since the equilibrium degree of order depends on temperature, WQ and FC samples annealed at the same SecHT temperature should approach, over time, to the same state of order. However, these samples start from opposite states. As a consequence, FC samples disorder (relative to their highly ordered state) upon secondary heat treatment, while the opposite happens to the WQ samples. Fig. 12 demonstrates that although WQ and FC samples tend to the same T_C^A value, they present distinct evolution after the initial 0.25 h of SecHT. T_C^A for the WQ samples evolves slowly towards equilibrium over a long period of time while for FC samples, the T_C^A is stabilized to its equilibrium value over very short times. The very different times required to achieve equilibrium suggests a marked asymmetry in the order/disorder kinetics, depending on the direction of the reaction.

The results, however, are somewhat counterintuitive as previous work on the ordering kinetics in Ni-Mn-Al alloys [101] suggest that ordering for FC samples should be slower than for water quenched ones. The reasoning is that WQ samples have quenched-in vacancies that enhance atomic mobility and should thus increase the rate of the order/disorder reaction. Since it is clear that the FC samples reached equilibrium within very short times, one can assume that atomic ordering processes are sufficiently fast. These atomic processes are expected to be invariant with regards to the direction of the reaction so they can be expected to be equally fast in the WQ samples. The slow kinetics in the evolution of T_C^A for the WQ samples thus may have an origin that is not dependent on the rate of atomic exchange between In and Mn atoms.

The results are also counterintuitive from another point of view: T_C^A is a direct proxy for degree of order. Since WQ samples have lower T_C^A than FC samples––until they converge after long heat treatment times––they should have a lower degree of order. A lower degree of order would decrease the stability of the austenite and would result in a higher M_S for the WQ samples as compared to the FC samples. However, M_S of WQ samples is in fact 35 K and 53 K lower than the corresponding FC samples, respectively, as shown in Fig. 9. Once again, the underlying reason for the behavior of M_S in the WQ samples seems to be related to features that go beyond the atomic scale.

Besides the evolution of overall degree of order, there should exist a second mechanism/microstructural feature that would be able to explain the increase in M_S after achieving M_S minimum, while also being compatible with the slow evolution of T_C^A for the WQ samples. Bruno *et al.* [46] suggested that such microstructural feature could be the annihilation of quenched-in vacancies. However, recent numerical simulations by the present authors [105,118] have shown that although the vacancy annihilation process is slower than the atomic exchange associated with ordering, it is still much faster than the timescales associated with the evolution of the non-monotonic dependence of M_S with SecHT time.

Summarizing the above observations and discussions, one can assume that: i) overall degree of $L2_1$ order should be stable after the first 0.25 h of SecHT for WQ and FC samples; ii) a possible change in the overall order or vacancy concentration can only play a role in the very early stages of the dependence of M_S with SecHT time, and cannot be the origin of the non-monotonic behavior of M_S; and even more, iii) they cannot be the major contribution to M_S change *neither before nor after* the M_S minimum. Therefore, we need to search for a more plausible mechanism that can explain both the decrease and increase of M_S temperature during long periods of time. Since overall degree of order is discarded, one should investigate possible microstructural factors affecting the thermostability of the phases.

4.2. Compositional effects

Figs. 6 and 11 clearly show how small changes in composition have a significant impact on the properties of both the MT and the ferromagnetic transition of the austenite. It is thus natural to briefly consider possible local compositional variations during the

thermal processes that could explain the SecHT time dependencies of M_S and T_C^A temperatures. The observed dependence of M_S and T_C^A on nominal change of Mn/In ratio in the solution heat treated and WQ conditions is in good agreement with previous works. Substituting Mn by In atoms decreases the density of valence electrons, increasing lattice stiffness [119]. This effect is expected to decrease MT temperatures, increasing T_C^A-M_S and reducing total entropy change during the MT. The latter effect explains why samples with higher In-content were more likely to show partial or full MT arrest. In turn, T_C^A may change only slightly on increasing In-content, since two compensating effects are expected: a decrease in the ferromagnetic interactions between the Ni(Co) and Mn atoms, reducing Curie point as observed in Fig. 11 [47]; and a slight increase of the overall degree of order as ODO temperature increases, increasing Curie temperature [120].

The composition of PC In13.5 for WQ, WQ+573K168h and FC samples was measured using a Cameca SXFive electron microprobe using Wavelength Dispersive X-ray Spectroscopy (WDS) in order to determine the possible effect of thermal processing on material composition. No significant change in composition was found either between different samples, or between different grains within the samples. Simultaneously, the samples were observed by scanning electron microscopy and no precipitate phases were observed even in the FC samples. Furthermore, diffraction patterns from different experiments, including the synchrotron radiation results used in this work as well as previous TEM observations [46], did not show extra peaks or peak broadening/split that could be associated with the formation of domains with different composition (and thus lattice parameters). For in-situ XRD experiments at temperatures between 675 K and 815 K for both WQ and FC samples, lattice parameter of the cubic austenite did not show any clear trend with a standard deviation below 0.02%. Such experimental evidence seems to discard the possibility of phase decomposition.

Nevertheless, Niitsu et al. [121] were able to detect micro-segregation of In atoms into the AntiPhase Domain Boundaries (APBs) for a $Ni_{50}Mn_{20}In_{30}$ alloy. In their work, an In-rich sample was annealed at 873 K for 168 h achieving a low density of APBs. Using HAADF-STEM and EDX, Niitsu et al. calculated a maximum of 2.7 at.% additional In content on the center of a 24 Å width APB as compared to the composition of the ordered domain. If we assume a similar micro-segregation process in the present Ni-Co-Mn-In samples close to M_S minimum, which demonstrate $L2_1$ domains with average length-scale about 300-400 Å, 24 Å APBs would represent around 16-21% of the sample volume, and an 1.35 at.% average segregation of Mn along APBs volume could results on a variation of average 0.25-0.35 at.% Mn/In change on the ordered $L2_1$ domains. Such a compositional change would be expected to notably decrease the transformation temperatures. One could hypothesize that the decrease of the MT temperatures, before M_S minimum, is caused by gradual segregation of Mn into the APBs, changing the composition of the domains. Such micro-segregation process cannot be excluded with current experimental evidences because WDS measurements result from averaging the composition over an area of the order of few micrometers. Still, any compositional change would need to be small enough not to be detected by the in-situ evolution of lattice parameters. In addition, we should consider the different thermal history of the samples. For $Ni_{50}Mn_{20}In_{30}$ alloy [121], a long heat treatment of 168 h was performed below ODO temperature, where order domains and APBs exits and segregation could proceed over time. In the present work, however, WQ samples were solutionized for 24 h above ODO temperature, so $L2_1$ order domains and APBs had to be produced during quenching and following SecHTs. Starting from WQ state and comparing with SecHTs performed at lower temperatures, M_S minimum state should have been reached in a few minutes at 873 K. Therefore, the evolution of MT temperatures and micro-segregation process may have quite different time-scales.

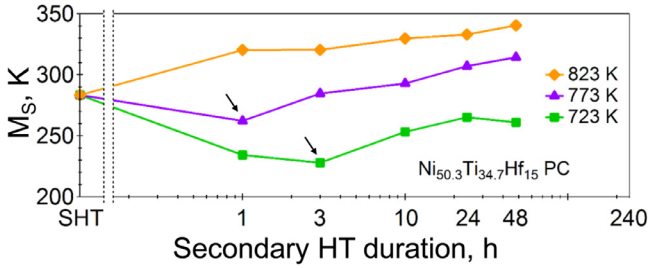

Figure 13. Martensite start (M_S) temperature after solution heat treatment at 1173 K for 1 h, followed by secondary heat treatments of different duration and temperature, 723 K (green squares), 773 K (purple triangles) and 823 K (orange diamonds) $Ni_{50.3}Ti_{34.7}Hf_{15}$ SMAs. Arrows indicate the position of M_S minimum. Data was originally published in [114].

Çakır et al. have shown the decomposition of Mn-rich Ni–Mn–In alloys [122–124], being this process quite fast for low In-content ($Ni_{50}Mn_{45}In_5$), but almost undetectable for $Ni_{50}Mn_{30}In_{20}$. Following these works, the present alloys would be expected to decompose into FM Ni_2MnIn-like and AFM NiMn-like domains. Such process would increase In-content of the matrix, resulting in a decrease of M_S. The effect on T_C^A is harder to predict since it would be determined by the redistribution (or not) of Co atoms and the magnetic interactions of the matrix with the incipient and more AFM Ni-Mn-like precipitates. Then, only the SecHT time dependence of WQ samples before M_S minimum seems compatible with a compositional effect, while, after M_S minimum, MT temperatures change should necessary be related with another mechanism. In conclusion, i) there is no experimental evidence of composition variation in present $Ni_{50}Co_5Mn_{50-X}In_X$ alloys and ii) the composition effect cannot explain, by itself, the entire experimental observations.

4.3. Microstructural size effects: Precipitates

Different SMAs, such as Fe-Ni-Al [125], Ni-Ti [126] and Ni-Ti-Hf alloys [114], have been previously shown to present a non-monotonic dependence of the MT temperatures on SecHT time as the consequence of a precipitation reaction occurring during such secondary heat treatments. For instance, Fig. 13 presents the dependence of M_S on SecHT temperature and duration for $Ni_{50.3}Ti_{34.7}Hf_{15}$ alloy. The comparison between Figs. 6 and 13 reveals notable similarities: i) for the same SecHT duration, M_S increases with SecHT temperature; ii) below certain SecHT temperature, time-dependence of M_S presents a minimum; and iii) the time required to achieve M_S minimum increases on decreasing SecHT temperature. Despite the fact that no second phases were found on Ni-Co-Mn-In alloys, as detailed in the previous section, it is important to explore the origins of such similar behaviors: what microstructural features at length scales beyond local fluctuations in composition and/or order parameter can affect the onset of the MT?

In precipitation-strengthened SMAs, there is a mechanical effect generated by the interaction, via local heterogeneities in strain fields, between the precipitates and nucleation and growth of the MT. In such systems, during the SecHT processes, small secondary phase particles precipitate from the matrix, leading to high particle density populations with very small interparticle spacings. This small interparticle distance can be comparable to the critical nucleus size of the martensite and this increases the energy barrier that the MT nucleus must overcome in order to propagate throughout the austenite matrix. To overcome such increasing barriers a more significant undercooling is required, thus decreasing the M_S

temperature. In some cases, the energy barriers can be sufficiently high to completely arrest the MT. As precipitates coarsen upon further annealing, the barriers to the MT decrease and the M_S recovers, as shown in Fig. 13 for the case of the Ni-Ti-Hf precipitation strengthened SMA. Fig. 13 seems to be analogous to Fig. 6 and while the presence of nano-precipitates has been discarded in the investigated Ni-Co-Mn-In alloys, there are other microstructural processes that evolve over diffusive times and that can exist at length scales that could interfere with the onset of the MT.

4.4. Evolution of $L2_1$ atomic order domains

On decreasing temperature below the critical temperature, $T_{B2\text{-}L21}$, the second order B2→$L2_1$ ordering transition should occur by successive local rearrangements. These successive rearrangements should lead to a continuous series of intermediate states which progressively increases the stability of the system and the order parameter. This process requires time as it is controlled by the kinetics of the atomic diffusion of Mn and In atoms through thermally activated jumps. The crystal can gain high overall degree of $L2_1$ order with a relatively small number of thermally activated jumps. However, B2 symmetry can be broken into two equivalent $L2_1$ states depending on the stacking order of Mn and In atoms.

Consequently, during the beginning of the ordering process, initial local rearrangements will randomly select one of the two equivalent $L2_1$ phases, producing a microstructure with many antiphase domains of nanosize length scales. The crystal then will contain many APBs and antisite defects. These defects/microstructures have positive excess free energy, so the system will reduce the total area and curvature of APBs by growing/coarsening the $L2_1$ order domains over time. Interestingly, the coarsening process may require a much larger number of thermally activated atomic jumps than those required for achieving the thermal equilibrium degree of order and may have a weaker driving force, so coarsening can span over longer periods of time than the evolution of overall degree of order observed in Fig. 10.

To gain further insight on the coarsening process during the heat treatments, the synchrotron transmission XRD experiments were performed on PC In13.3 WQ samples. Two different experimental procedures were used. In the first one, in-situ samples were in solution heat treated condition at the start of the experiments and, as for those shown in Fig. 10, heated from room temperature to different target temperatures and held at those temperatures for a period of time while performing XRD scans at regular time intervals. For the second procedure, Pre-SecHT samples had already been secondary heat treated and water quenched to room temperature, and their diffraction spectrum was obtained in the austenite state at 423 K. Regardless of the nature of these two kinds of experiments, Fig. 14 suggests very little difference in the time evolution of the characteristic length scale of $L2_1$ domains, L. This observation indicates that the quenching process after the secondary heat treatments does not have a significant effect on the final average domain size for heat treatment temperatures below 773 K, i.e. for the same range of temperatures that present non-monotonous dependence of MT characteristics on SecHT time.

In general, L presents a strong dependence in both annealing time and temperature. Average domain size for the in-situ sample annealed to 675 K increases only slightly during the heating process to 675 K, from around 90 Å to 115 Å. However, coarsening accelerates on continuing heating, so the in-situ sample annealed to 815 K achieved a characteristic length scale L of around 200 Å before it was held isothermally. Once entered in the isothermal stage, the ordered domain size increased following a power law, $L \propto t^n$, in which the exponent n depends on temperature and seems to decay over time while L coarsens towards a temperature-dependent saturation size. Early exponent n for PC in-situ samples annealed at 675, 750 and 810 K was around 0.3, 0.5 and >1, respectively.

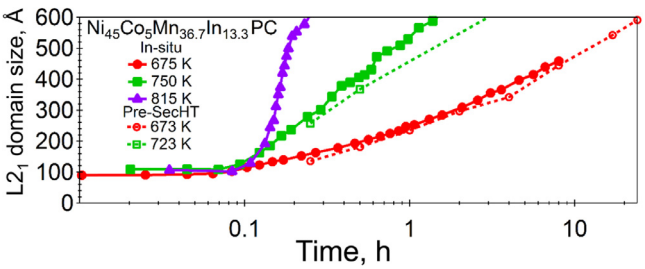

Figure 14. Average $L2_1$ order domain size as calculated from the width of the $(111)_{L21}$ diffraction peaks for polycrystalline $Ni_{45}Co_5Mn_{36.7}In_{13.3}$. Data from in-situ experiments performed at the indicated temperatures is represented with full symbols-solid lines, while data from the pre-heat treated samples is shown with open symbols-dashed lines. Note that color represent curves with similar temperature, but not the same. In-situ samples were initially solution heat treated and then secondary heat treated while doing in-situ synchrotron measurements at certain time intervals. The Pre-SecHT samples were heat treated at the given heat treatment for specific durations shown in the figure and then water quenched to freeze in the order at that temperature. The synchrotron measurements were performed at 423 K on the Pre-SecHT samples.

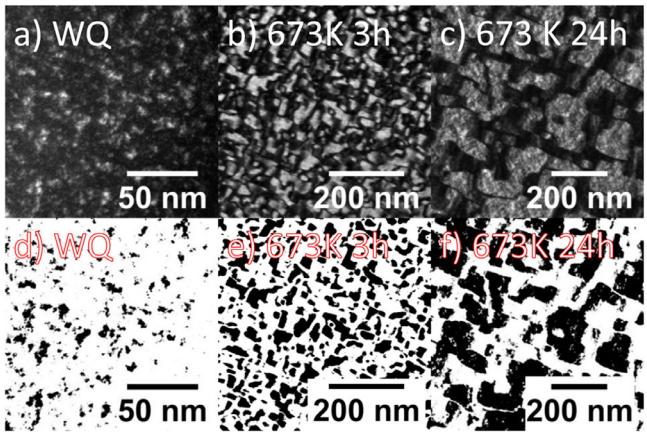

Figure 15. $(111)_{L21}$ dark-field micrographs collected in the (011) cubic austenite zone axis for $Ni_{45}Co_5Mn_{36.6}In_{13.4}$ SC samples with (a) only solution heat treatment followed by water quenching (WQ) or with additional secondary heat treatments at 673 K for (b) 3 h and (c) 24 h. Note that the magnification is different for the different images. (d)-(f) The same images processed for domain size determination. These micrographs were published in [46].

Such temperature dependence was unexpected since a typical second order transition which is diffusion based and "curvature driven" is usually found to follow a Lifshitz-Allen-Cahn growth [127], which is proportional to $t^{1/2}$. This rate, at least in the early coarsening stage, should be temperature independent. However, the present results deviate from this behavior, especially in the case of the sample annealed at 675 K, which shows slow kinetics (n<0.5) during 8 h of the experiment. The strong dependence of the exponent n on temperature suggests that the coarsening mechanism should depend on temperature as well. The origin of this phenomenon would be the focus of a future work.

In order to corroborate the average ordered domain size calculated using diffraction peak broadening, we have analyzed the $L2_1$ ordered domains as observed using (111) dark field mode in TEM. Figure 15 presents the dark field micrographs of SC In13.4 samples after different thermal procedures: a) SHT WQ, b) WQ + 673K3h and c) WQ + 673K24h, which were originally published in ref. [46]. These images should correspond to microstructural states approximately equivalent to the PC In13.3 WQ sample in-situ heat treated to 675 K in Fig. 14. At first glance, $L2_1$ order domains, bright regions in Figs. 15a-c, clearly coarsen over time when the material

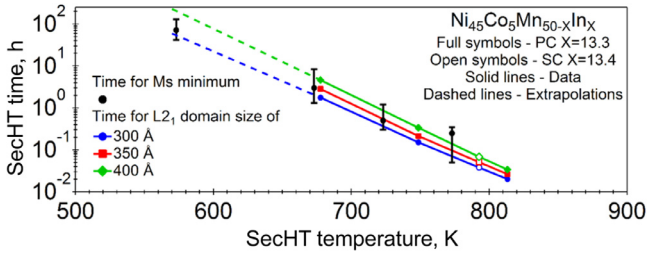

Figure 16. Comparison between the time necessary to minimize M_S temperatures at different secondary heat treatment temperatures, black circles, and time required to obtain an average $L2_1$ domain size of 300 Å, blue circles, 350 Å, red squares, and 400 Å, green diamonds, as a function of secondary heat treatment temperature. Error bars point out the uncertainty of M_S minimum determination because of the low density of data points. Dashed lines extrapolate the dependence of the average domain size on temperature to 573 K.

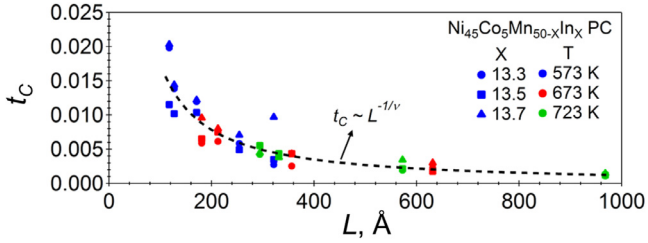

Figure 17. Size dependence of the reduced Curie temperature shift $t_C=(T_C(\infty)-T_C(L))/T_C(\infty)$ for polycrystalline WQ $Ni_{45}Co_5Mn_{50-X}In_X$ MMSMAs in austenite phase with X=13.3 (circles), 13.5 (squares) and 13.7 (triangles) samples secondary heat treated at 573 K (blue), 673 K (red) or 723 K (green) for different times. Dashed line presents a power law fitting.

is secondary heat treated at 673 K. This coarsening process was quantified by calculating the average $L2_1$ order domain size using ImageJ software [128]. The distinction between ordered and disordered regions was established choosing a threshold intensity value for each image, as shown in Figs. 15d-f. Approximated average sizes for SC In13.4 samples are 50-60 Å for WQ, 250-270 Å for WQ + 673K3h and 680-700 Å for WQ + 673K24h cases. In comparison, the values obtained using XRD peak broadening method are 50 Å for SC In13.4 WQ sample, 80, 350 and 590 Å for PC In13.3 WQ, WQ + 673K3h and WQ + 673K24h samples, respectively. Differences in sizes between single crystalline and polycrystalline WQ cases may be related with different effective cooling rates during the quenching process, which should produce different $L2_1$ overall order and domain size.

In addition, PC In13.3 FC samples were also used in the in-situ experiments, equivalent to the ones shown in Fig. 14 for WQ samples. During both heating and isothermal stages of these experiments, the peak broadening was always equivalent, within scattering, to the one of LaB_6 standard sample. This fact indicates that domain size peak broadening of FC samples was negligible and thus average size of the $L2_1$ domains was large, above 1000 Å, during the thermal processes. Consequently, it was not possible to measure accurately the heat treatment time evolution of L on the FC samples with this experimental technique, and for this reason, these data are not presented in Fig. 14.

Note that initial domain size of FC samples was expected to be large because of the controlled slow cooling at 0.55 K/min. The negligible peak broadening during heating experiments demonstrate that, despite of the ongoing disordering process, the order domains didn't reduce their average size to measurable levels. Therefore, these results point out a significant difference in the SecHT duration dependence of the microstructures of WQ and FC samples: only WQ samples present $L2_1$ order domain sizes at the nanoscale.

4.5. Microstructural size effects: $L2_1$ order domain size

By comparing Figs. 6, 12 and 14, it is evident that the evolution in M_S, Curie temperature and $L2_1$ order domain length scale L span similar time scales in the WQ samples. Figure 16 presents a comparison between the SecHT time required to achieve M_S minimum, t_{MS}, as seen in Fig. 6, with the SecHT temperature dependence of time necessary to achieve different average $L2_1$ domain sizes, 300 Å, 350 Å and 400 Å, t_{L21}. To account for the heating rate effect on the calculated time, a constant level of 8 min has been subtracted from the latter. After this correction, data presents a good linear fit between SecHT temperature and $\log(t_{L21})$. Error bars on t_{MS} data are based on the experimental SecHT time intervals. Given the uncertainty on t_{MS} data, the precision of such calculation is relatively low, but the similar correlation between t_{MS} and t_{L21} is observed for data at 673 and 723 K, where t_{MS} data lie slightly below 350 Å line. Note that these two cases are the most reliable, because their coarsening rate was suitable for the in-situ experiments. Even though the comparison between t_{MS} and t_{L21} at 573 K can only be done through the extrapolation, t_{MS}(573 K) lies above extrapolated 300 Å line, being in the same size range as other data points.

Overall, and considering the uncertainty in t_{MS} data, the minimum of the non-monotonous behavior of the time-dependence of MT temperatures on WQ samples is correlated to the existence of intermediate average $L2_1$ order domain sizes between 300 and 400 Å, likely close to 350 Å, suggesting that this behavior is, in fact, a size effect. Note that this critical length scale depends on the assumed shape of the domains, factor K in the Scherrer equation, based on the TEM images [46]. Interestingly, L for FC samples during SecHTs is in all cases well above 300–400 Å size range (likely above 1000 Å), which may explain the absence of non-monotonous behavior (size effects) in these samples, Fig. 10.

Furthermore, evolution of average $L2_1$ domain size may also explain the different time dependence of T_C^A in WQ and FC samples. As shown in Figs. 11 and 12, T_C^A in WQ samples increased slowly over time, especially for 573 and 673 K cases, while in FC samples T_C^A is completely SecHT time independent. As a consequence of occurring in a finite medium, the second order PM→FM transition cannot occur sharply at a certain T_C^A ($L=\infty$) [129]. Instead, the transition peak will be rounded and shifted to T_C^A (L). Such shift can be significant when the characteristic microstructural length scale decreases to become comparable to the characteristic magnetic length scale [130]. The dependence of the second order magnetic transition temperature on crystallite size is expected to be described by the critical exponent ν as $t_C=(T_C(\infty)-T_C(L))/T_C(\infty)\sim L^{-1/\nu}$, where t_C is the reduced Curie temperature shift due to the length scale of the magnetic domains [130].

Figure 17 shows the comparison between the calculated reduced Curie temperature shift, t_C, and the estimated average size of the $L2_1$ order domains, L, for the PC WQ MMSMA samples used in Fig. 11. Samples annealed at 773 K are skipped since no net T_C^A change with annealing time is observed in Fig. 11 and large domains are expected after the first 0.25 h of secondary heat treatment. Fit in Fig. 17 gives a critical exponent ν of 0.86±0.05 (1σ). This value is larger than the critical exponent ν for a 3-dimensional vector Heisenberg model for isotropic magnets (ν=0.71) [131]. Different phenomena can deviate the size-dependent critical exponent from the theoretical value, like surface effects or magnetic anisotropy. However, both L and $T_C(\infty)$ data are indirectly estimated and scattering is significant, being one standard deviation (1σ) around 6% of the calculated value. Nevertheless, the correlation between t_C and L observed in Fig. 17 is compatible with a possible interaction between the average length

scale of the $L2_1$ order domains and the characteristic length scale of the magnetic domains.

Summarizing the line of arguments presented above, we have shown that the SecHT time dependence of WQ and FC samples of both MT temperatures and T_C^A are different, Figs. 9 and 12, where WQ presented a non-monotonic behavior for M_S and slow increase for T_C^A, while FC samples were time-independent. The explanation for such behaviors should lie on the microstructural evolution of the material during the secondary heat treatment process. There is no experimental evidence of compositional variations, neither phase separation nor micro-segregation. Even if undetected, a hypothetical composition effect cannot explain, by itself, the non-monotonic behavior of M_S temperature. Average degree of $L2_1$ order and vacancy concentration achieves thermal equilibrium levels in time scales shorter than the evolution of M_S and T_C. The only notable demonstrated difference between the microstructures of WQ and FC samples and its dependence on SecHT duration lies in the $L2_1$ order domain coarsening process. In addition, SecHT time dependence of both M_S and T_C^A of WQ samples present a correlation with the average $L2_1$ order domain size.

Altogether, we suggest that sufficient evidence of the existence of atomic order microstructure-related size effects on martensitic transformation characteristics of MMSMAs has been gathered. However, the available experimental data do not permit us to deduce the interaction mechanism between the martensitic transformation and the order domain microstructure. Our hypothesis is that certain atomic order microstructural configurations (and especially those with average order domain size between 300 and 400 Å) produce elastic energy barriers to the transformation. In particular, the MT may be significantly hindered by the microstructure when the critical nucleus radius required for the formation of martensite plates has dimensions comparable to average order domain size.

4.6. Thermodynamic modeling of magneto-thermo-mechanical transitions

Following Classical Nucleation theory (CNT), the energy barrier that needs to be overcome in order to form a stable nucleus of martensite within the parent phase will depend on nucleus shape, its dimensions as well as elastic interactions between the nucleus and the matrix. Kurdjumov and Ruitburd [1,132] demonstrated that for a thin plate-like martensitic nucleus of side length L, diagonal D and thickness H, the critical dimensions D* and H* that minimizes the energy barrier can be approximated as:

$$D^* = \frac{8\sqrt{2}}{3}\frac{\gamma e_L}{\Delta F^{*2}} \quad (1)$$

$$H^* = \frac{4}{3}\frac{\gamma}{\Delta F^*} \quad (2)$$

where γ is the interfacial energy at the austenite-martensite boundary, e_L is the specific energy of the elastic field close to the plate nucleus edge and ΔF^* is the effective thermodynamic driving force for the nucleation of martensite. Following [132], we have approximated e_L as $e_L = Gu_0/\pi$, where G is the shear modulus of the austenite and u_0 is the transformation strain. These properties were evaluated using the elastic parameters in Ref. [133]. In turn, the effective driving force for nucleation has been estimated as the difference between the reversible terms of the MT free energy difference and an irreversible contribution that accounts for energy losses occurring during the MT, $\Delta F^* = \Delta F_{REV} - \Delta F_{IRR}$. To evaluate the reversible transformation thermodynamic free energy, we have utilized the recent model developed by L'vov *et al.* [133] based on Landau theory of phase transitions to investigate the magnetostructural transformation in Ni–Co–Mn–In MMSMAs. In this model, the free energy difference between austenite (FM phase) and martensite (AFM phase) accounts for magnetic (m), elastic (e), and magneto-elastic (me) contributions:

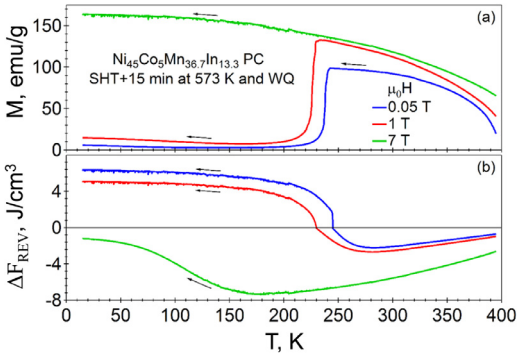

Figure 18. Temperature dependence of the (a) experimental magnetization and (b) calculated reversible free energy difference for a polycrystalline $Ni_{45}Co_5Mn_{36.7}In_{13.3}$ sample secondary heat treated at 573 K for 0.25 h during cooling under different constant applied magnetic fields: 0.05, 1 and 7 T. Arrows show the direction of the temperature ramp.

$$\Delta F_{REV} = F_{FM} - F_{AFM} = \Delta F_m + \Delta F_e + \Delta F_{me} \quad (3)$$

$$\Delta F_m = \frac{1}{2}J(T){M_0}^2(T) - M_0(T)H + \frac{1}{2}M(T,H)H \quad (4)$$

$$\Delta F_e + \Delta F_{me} = -\frac{1}{2}c_2(T,H){u_3}^2 - \frac{1}{3}a_4(T,H){u_3}^3 - \frac{1}{4}b_4{u_3}^4 \quad (5)$$

in which J is the magnetic exchange interaction, M_0/M are the saturation/total magnetization, respectively, H is the magnitude of applied magnetic field, c_2, a_4 and b_4 are modified Landau coefficients, and u_3 is the Landau order parameter. Please, see ref. [133] for the detailed formulation of these parameters and properties. Figure 18 presents an example of the calculated reversible free energy difference for a PC In13.3 WQ 573K0.25h sample during cooling under different applied magnetic fields. As expected, MT driving force decreases on increasing applied magnetic field till it is negative for the entire temperature range under 7 T, leading to the thermodynamic arrest of the austenite.

This arrest phenomenon is a consequence of the severe reduction in the MT total entropy difference, Δs [98,99]. For a set of PC In13.3, In13.5 and In13.7 samples with various thermal histories and transformations under different applied magnetic fields (0.05, 1 or 7 T), Δs has been calculated both from calorimetric data, $\Delta s^{DSC} = \int \delta q/T$, where q is the transformation exchange heat, and from magnetic data, $\Delta s^{SQUID} = \Delta m(\partial H/\partial M_S)$, where Δm is the magnetization difference between austenite and martensite phases and $\partial M_S/\partial H$ is the shift in the transformation temperatures with applied magnetic field. Note that Δs^{DSC} was calculated by averaging the response from forward and reverse transformations, while Δs^{SQUID} was calculated at M_S and M_F temperatures. These data are presented in Fig. 19a. Both calculations of the entropy change exhibit similar values and dependence on the T_C^A-M_S difference. The entropy difference at M_F is a bit lower than that at M_S, as the magnetization of austenite increases with decreasing temperature. Interestingly, $\Delta s^{SQUID}(M_F)$ reaches a saturation level at T_C^A-M_S values above 190 K. This range of T_C^A-M_S values corresponds to the set of samples that typically exhibits partial martensitic transformation. For these cases, experimentally determined M_F is the temperature at which MT entropy difference becomes very small and it is not possible to achieve the MT driving force level required for continuing the forward transformation. This leads to a mixture of austenite and martensite phases at low temperatures. The observed evolution of Δs has a significant impact on MT thermal hysteresis, calculated as $\Delta T = (A_F + A_S - M_S - M_F)/2$. As shown on Fig. 19b,

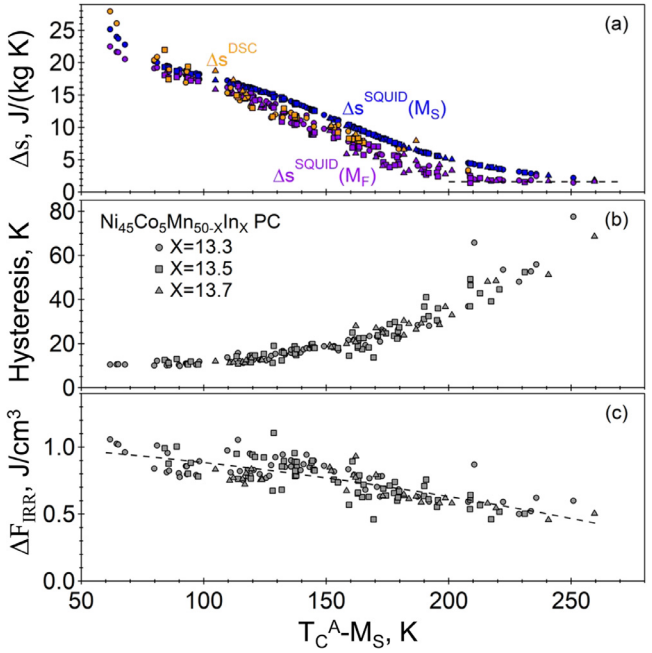

Figure 19. (a) Total entropy difference for the martensitic transformation calculated from DSC data (orange) and from thermomagnetic data evaluated at M_S (blue) and M_F (purple), (b) martensitic transformation thermal hysteresis and (c) estimated irreversible martensitic transformation free energy for the polycrystalline $Ni_{45}Co_5Mn_{50-X}In_X$ MMSMAs with X=13.3 (circles), 13.5 (squares) and 13.7 (triangles) and with different thermal processing conditions and under different applied magnetic fields. Horizontal dashed line in (a) shows the saturation of entropy difference at M_F for partial martensitic transformations and dashed line in (c) shows the best fit line used for the calculation of ΔF^*.

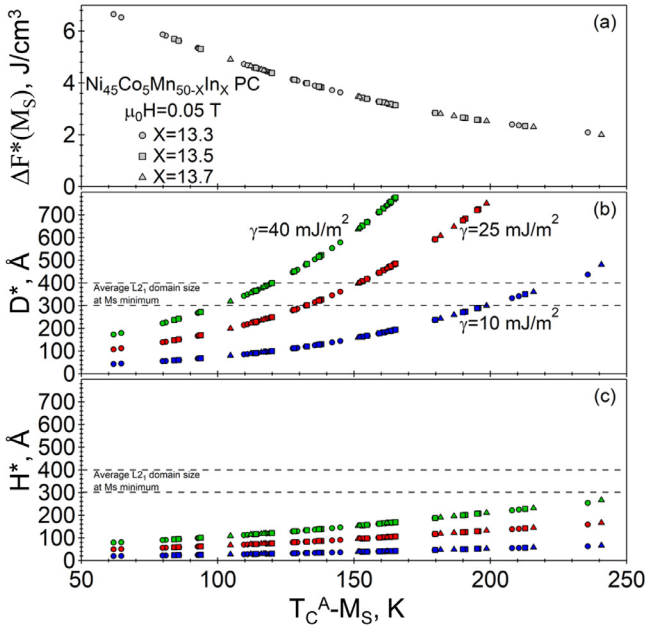

Figure 20. (a) Calculated martensitic transformation free energy difference at M_S temperature and critical (b) diagonal D^* and (c) thickness H^* of a martensite plate nucleus for different values of interfacial energy, γ=10 (blue), 25 (red) or 40 mJ/m^2 (green), for the direct MT (cooling, constant magnetic field of 0.05 T) in polycrystalline $Ni_{45}Co_5Mn_{50-X}In_X$ MMSMAs with X=13.3 (circles), 13.5 (squares) and 13.7 (triangles) and with different thermal processing conditions. Horizontal dashed lines delimit the calculated range of the critical average $L2_1$ order domain size for comparison.

thermal hysteresis displays a monotonic increase with increasing T_C^A-M_S difference. One can note that neither MT entropy difference nor thermal hysteresis exhibit a significant dependence on composition, in the composition range studied here, pointing out once again the strong dependence on the magnetic entropy difference between austenite and martensite phases. Then, as the total entropy difference decreases, the amount of undercooling required for achieving certain value of MT driving force increases.

Next, we have employed the experimental data for the MT entropy change and thermal hysteresis to estimate the value of the irreversible MT free energy, ΔF_{IRR}. Following Panchenko et al. [126], the energy losses associated with the friction stresses required for the motion of the transformation interface and the plastic relaxation of the elastic energy due to the formation of crystalline defects can be approximated as:

$$\Delta F_{IRR} = \frac{1}{2}\Delta s \Delta T \tag{6}$$

This term was evaluated at M_S temperature for PC (In13.3, In13.5, In13.7) samples. As it can be observed on Fig. 19c, the estimated irreversible free energy difference presents a weaker dependence on temperature as compared to MT entropy change and hysteresis, decreasing on increasing T_C-M_S difference.

Figure 20a shows the effective free energy for nucleation, $\Delta F^* = \Delta F_{REV}$ - ΔF_{IRR}, evaluated at M_S temperature for PC (In13.3, In13.5, In13.7) samples after different thermal processing conditions under 0.05 T. For this calculation, we have used the experimentally obtained values for M_S, T_C^A, saturation magnetization, MT magnetization change, MT entropy change and hysteresis; and estimated critical magnetic field for reverse martensitic transformation and elastic coefficients from ref. [133]. Note that scatter in the ΔF^* values is significant due to the variability of some of the experimentally measured properties, such as the magnetization change during MT; thus we have utilized fitted curves, such as the dashed line in Fig. 19c, for obtaining a clear picture of the order of magnitude and temperature dependence of the properties presented in Fig. 20. Since some of these properties, like hysteresis and critical magnetic field for inducing the transformation, depend strongly on the MT magnetic entropy difference, Δs_{mag}, the calculated effective MT free energy demonstrates a monotonic dependence on T_C^A-M_S. In other words, the MT driving force decreases as the magnetic entropy difference increases. Note that samples that did not transform (arrested) would appear at the right side of Fig. 20a; however, their theoretically higher T_C^A-M_S difference would have resulted in an insufficient MT driving force for overcoming the elastic energy barriers for the nucleation and growth of martensite.

We would like to point out that the evaluation of the austenite-martensite interfacial energy γ is not straightforward since it is normally indirectly inferred from related crystallographic phenomena. For example, Olson and Cohen [134] derived the interfacial energy of coherent FCC–HCP boundary in Fe–Cr–Ni alloy as half of the intrinsic stacking fault energy, giving a value within 10-15 mJ/m^2. On the other hand, Zhang *et al.* [135] assumed that nucleation and growth of martensite requires the formation of martensite twin-boundaries, and so the transformation interfacial energy should account for twin-boundary energy in addition to bulk elastic stored energy and bulk austenite-martensite free energy difference. Using these considerations, they selected 25 mJ/m^2 for the contribution of martensite twins to the transformation interfacial energy in their work on the investigation of MT hysteresis on Ni-Ti-based SMAs. Similarly, in the case of ferromagnetic Ni-Mn-based alloys, O'Handley *et al.* [136] determined that the interface energy of martensite twin-boundaries formed during cubic-to-tetragonal ferromagnetic transformation in Ni-Mn-Ga alloys was about 40 mJ/m^2, taking into account the Zeeman energy change across the martensite twin boundary.

None of the cases above are fully equivalent to the scenario on $Ni_{45}Co_5Mn_{50-X}In_X$ alloys as martensite twins are weakly magnetic, likely decreasing twin-boundary energy as compared to Ni-Mn-Ga, but there should be an enhanced Zeeman energy contribution at the FM austenite – PM martensite interface. To be able to estimate the critical nuclei dimensions, we have assumed that 10–40 mJ/m^2 is an appropriate range to delimit the order of magnitude of the MT interfacial energy on Ni–Co–Mn–In alloys. Figures 20b and 20c present an estimation of the martensite nucleus critical dimensions, D^* and H^*, using the calculated effective MT free energy difference, Fig. 20a, and different values of interfacial energy γ. Note that the temperature-dependencies of D^* and H^* observed in Fig. 20 are not reliable because γ is expected to have a weak dependence on T_C^A-M_S because of the variation of Zeeman energy at the interface. Notably, following CNT, the average $L2_1$ order domain size at M_S minimum, i.e. the average distance between antiphase domain boundaries, is of the same order of magnitude as the roughly estimated diagonal D^* of the martensite plate-like critical nucleus, which should be its largest characteristic length. In turn, the estimated thickness of the critical nucleus H^*, in Fig. 20c, may be sensibly smaller than the critical average $L2_1$ order domain size, and this means that the nucleus should be less likely to interact with antiphase boundaries along the thickness direction. Altogether, calculations reinforce the possible existence of interactions between the atomic order microstructure and the martensitic transformation, which may account for the observed non-monotonic dependence of MT properties on heat treatment duration.

5. Summary and Conclusions

The main contribution of the present work is the experimental investigation of order domain coarsening phenomenon and its effects on the martensitic transformation (MT) characteristics in Ni–Co–Mn–In MMSMAs. These microstructural size effects have been demonstrated through the correlations between thermal processing parameter dependence of the average order domain size L and both the martensitic transformation M_S and the Curie temperature T_C^A. The evolution of L was investigated via in-situ high-energy XRD diffraction experiments and TEM observations, while M_S and T_C^A evolutions were monitored through a systematic investigation of their dependence on composition, thermal processing parameters and applied magnetic field. Finally, theoretical estimations for the MT free energy were performed to calculate the magnitude of the critical nucleation dimensions (in the framework of the classical nucleation theory). These calculations suggest that atomic order domain size effects have their origin in the elastic interaction between the martensite nuclei and antiphase boundaries.

The MT characteristics, in particular the transformation temperatures, in Ni–Co–Mn–In MMSMAs are a complex function of composition, through its effect on magnetism and elastic stiffness; atomic order microstructure, through its impact on magnetism and the mechanical interaction between mesoscale atomic order domains and the MT microstructural features; and of applied external magnetic (or stress) field, through its direct (indirect) impact on the phases' magnetism and thermostability. Increase in average atomic order domain size over time has been demonstrated to result in unexpected non-monotonic behavior of the MT temperatures. Other possible contributions, specifically other crystalline defect features like anti-site defects or grain boundaries, seem not to play a primary role on the change in martensitic transformation characteristics with thermal processing within the present work.

From the engineering point of view, the thermal processing variables controlling the martensitic transformation characteristics are the initial cooling rate, which changes overall degree of order and the average size of the atomic order domains; the secondary heat treatment temperature, which varies the overall degree of order to the thermal equilibrium spontaneous degree of order and modifies order domain size growth rate; and secondary heat treatment duration, which selects the overall degree of order (only for very short heat treatments at low temperatures) and, more significant, the final average size of the order domains for the water quenched samples. Altogether, secondary heat treatments can result in samples of different overall degree of order, for both WQ and FC samples, and different average order domain size, only for WQ samples, allowing us to largely modify the properties of these materials.

Many MT characteristics, such as transformation enthalpy change, transformation hysteresis, transformation range, and magnetization change upon transformation are dominated by the change in the magnetic free energy/entropy during the MT, which in turn is strongly correlated with the difference between the ferromagnetic transition and MT characteristic temperatures, T_C^A-M_S. The average $L2_1$ order domain size strongly affects all these MT characteristics, when below certain size (roughly about 40-50 nm), by controlling M_S, and thus T_C^A-M_S, since T_C^A is not as sensitive to the average $L2_1$ order domain size as M_S. In other words, the average $L2_1$ order domain size can control the MT magnetic free energy/entropy. As a consequence, many characteristics of MT in Ni–Co–Mn–In MMSMAs have a direct correlation with the average order domain size, similar to T_C^A-M_S.

The similarities between the order domain effects in Ni–Co–Mn–In MMSMAs and precipitation effects in other SMAs arise from the resemblance in the variation of order domain size and inter-precipitate distances with changes in SecHT temperature and time, and from analogous mechanical interactions between the MT microstructural features and the growing atomic order domains/precipitates.

Declaration of Competing Interest

The authors declare that they have no known competing financial interests or personal relationships that could have appeared to influence the work reported in this paper.

The authors declare the following financial interests/personal relationships which may be considered as potential competing interests.

Acknowledgements

Authors would like to acknowledge the financial support of the U.S. National Science Foundation through the grant DMR 1905325. YIC acknowledges the support from The Tomsk State University Competitiveness Improvement Program under the grant 8.1.06.2018. This research used resources of the Advanced Photon Source, a U.S. Department of Energy (DOE) Office of Science User Facility, operated for the DOE Office of Science by Argonne National Laboratory under Contract No. DE-AC02-06CH11357.

Supplementary materials

Supplementary material associated with this article can be found, in the online version, at doi:10.1016/j.actamat.2020.116616.

References

[1] A.L. Roitburd, G.V. Kurdjumov, The nature of martensitic transformations, Mater. Sci. Eng. 39 (1979) 141–167.
[2] R.J. Salzbrenner, M. Cohen, On the thermodynamics of thermoelastic martensitic transformations, Acta Metall 27 (1979) 739–748.
[3] J. Van Humbeeck, R. Stalmans, Shape Memory Behaviour, Mater. Sci. Forum. 56–58 (1990) 405–416.
[4] P. Wollants, J.R. Roos, L. Delaey, Thermally- and stress-induced thermoelastic martensitic transformations in the reference frame of equilibrium thermodynamics, Prog. Mater. Sci. 37 (1993) 227–288.

[5] T. Kakeshita, K. Kuroiwa, K. Shimizu, T. Ikeda, A. Yamagishi, M. Date, A New Model Explainable for Both the Athermal and Isothermal Natures of Martensitic Transformations in Fe-Ni-Mn Alloys, Mater. Trans. JIM. 34 (1993) 423–428.

[6] X. Huang, Y. Liu, Effect of annealing on the transformation behavior and superelasticity of NiTi shape memory alloy, Scr. Mater. 45 (2001) 153–160.

[7] K. Otsuka, X. Ren, Physical metallurgy of Ti–Ni-based shape memory alloys, Prog. Mater. Sci. 50 (2005) 511–678.

[8] H.Y. Kim, Y. Ikehara, J.I. Kim, H. Hosoda, S. Miyazaki, Martensitic transformation, shape memory effect and superelasticity of Ti–Nb binary alloys, Acta Mater 54 (2006) 2419–2429.

[9] E. Patoor, D.C. Lagoudas, P.B. Entchev, L.C. Brinson, X. Gao, Shape memory alloys, Part I: General properties and modeling of single crystals, Mech. Mater. 38 (2006) 391–429.

[10] B. Kockar, I. Karaman, A. Kulkarni, Y. Chumlyakov, I.V. Kireeva, Effect of severe ausforming via equal channel angular extrusion on the shape memory response of a NiTi alloy, J. Nucl. Mater. 361 (2007) 298–305.

[11] J. Ma, I. Karaman, R.D. Noebe, High temperature shape memory alloys, Int. Mater. Rev. 55 (2010) 257–315.

[12] K.C. Atli, I. Karaman, R.D. Noebe, A. Garg, Y.I. Chumlyakov, I.V. Kireeva, Shape memory characteristics of Ti49.5Ni25Pd25Sc0.5 high-temperature shape memory alloy after severe plastic deformation, Acta Mater 59 (2011) 4747–4760.

[13] N. Ozdemir, I. Karaman, N.A. Mara, Y.I. Chumlyakov, H.E. Karaca, Size effects in the superelastic response of Ni54Fe19Ga27 shape memory alloy pillars with a two stage martensitic transformation, Acta Mater 60 (2012) 5670–5685.

[14] A. Evirgen, I. Karaman, R.D. Noebe, R. Santamarta, J. Pons, Effect of precipitation on the microstructure and the shape memory response of the Ni50.3Ti29.7Zr20 high temperature shape memory alloy, Scr. Mater. 69 (2013) 354–357.

[15] J.A. Monroe, D. Gehring, I. Karaman, R. Arroyave, D.W. Brown, B. Clausen, Tailored thermal expansion alloys, Acta Mater 102 (2016) 333–341.

[16] D. Gehring, I. Karaman, Evolution of anisotropic and negative thermal expansion in rolled equiatomic nickel-titanium martensite, Scr. Mater. 186 (2020) 142–146.

[17] D. Gehring, J.A. Monroe, I. Karaman, Effects of composition on the mechanical properties and negative thermal expansion in martensitic TiNb alloys, Scr. Mater. 178 (2020) 351–355.

[18] J. Ma, I. Karaman, Self-adaptive, ultra-low elastic modulus shape memory alloys, US Patent: 9752219 (B2), 2017.

[19] J. Ma, I. Karaman, E. Flickinger, Variably flexible metal article and methods of making the same, US Patent: 10,538,835 (B2), 2020.

[20] L. Mañosa, D. González-Alonso, A. Planes, E. Bonnot, M. Barrio, J.-L. Tamarit, S. Aksoy, M. Acet, Giant solid-state barocaloric effect in the Ni–Mn–In magnetic shape-memory alloy, Nat. Mater. 9 (2010) 478–481.

[21] P.O. Castillo-Villa, L. Mañosa, A. Planes, D.E. Soto-Parra, J.L. Sánchez-Llamazares, H. Flores-Zúñiga, C. Frontera, Elastocaloric and magnetocaloric effects in Ni-Mn-Sn(Cu) shape-memory alloy, J. Appl. Phys. 113 (2013) 053506.

[22] Y.J. Huang, Q.D. Hu, N.M. Bruno, J.-H. Chen, I. Karaman, J.H. Ross Jr, J.G. Li, Giant elastocaloric effect in directionally solidified Ni–Mn–In magnetic shape memory alloy, Scr. Mater. 105 (2015) 42–45.

[23] A.M. Pérez-Sierra, N.M. Bruno, J. Pons, E. Cesari, I. Karaman, Atomic order and martensitic transformation entropy change in Ni–Co–Mn–In metamagnetic shape memory alloys, Scr. Mater. 110 (2016) 61–64.

[24] N.M. Bruno, S. Wang, I. Karaman, Y.I. Chumlyakov, Reversible Martensitic Transformation under Low Magnetic Fields in Magnetic Shape Memory Alloys, Sci. Rep. 7 (2017) 1–10.

[25] J.-H. Chen, N.M. Bruno, Z. Ning, W.A. Shelton, I. Karaman, Y. Huang, J. Li, J.H. Ross Jr, Relative Cooling Power Enhancement by Tuning Magneto-structural Stability in Ni-Mn-In Hesuler Alloys, J. Alloys Compd. 5 (2018) 785–790.

[26] X. He, S. Wei, Y. Kang, Y. Zhang, Y. Cao, K. Xu, Z. Li, C. Jing, Enhanced barocaloric effect produced by hydrostatic pressure-induced martensitic transformation for Ni44.6Co5.5Mn35.5In14.4 Heusler alloy, Scr. Mater. 145 (2018) 58–61.

[27] N.M. Bruno, I. Karaman, Y.I. Chumlyakov, Orientation Dependence of the Elastocaloric Effect in Ni54Fe19Ga27 Ferromagnetic Shape Memory Alloy, Phys. Status Solidi B. 255 (2018) 1700437.

[28] V.A. Chernenko, C. Seguí, E. Cesari, J. Pons, V.V. Kokorin, Sequence of martensitic transformations in Ni-Mn-Ga alloys, Phys. Rev. B. 57 (1998) 2659–2662.

[29] R. Tickle, R.D. James, Magnetic and magnetomechanical properties of Ni2MnGa, J. Magn. Magn. Mater. 195 (1999) 627–638.

[30] X. Jin, M. Marioni, D. Bono, S.M. Allen, R.C. O'Handley, T.Y. Hsu, Empirical mapping of Ni–Mn–Ga properties with composition and valence electron concentration, J. Appl. Phys. 91 (2002) 8222–8224.

[31] Y. Murakami, D. Shindo, K. Oikawa, R. Kainuma, K. Ishida, Magnetic domain structure in a ferromagnetic shape memory alloy Ni51Fe22Ga27 studied by electron holography and Lorentz microscopy, Appl. Phys. Lett. 82 (2003) 3695–3697.

[32] M.R. Sullivan, H.D. Chopra, Temperature- and field-dependent evolution of micromagnetic structure in ferromagnetic shape-memory alloys, Phys. Rev. B. 70 (2004) 094427.

[33] R. Kainuma, Y. Imano, W. Ito, Y. Sutou, H. Morito, S. Okamoto, O. Kitakami, K. Oikawa, A. Fujita, T. Kanomata, K. Ishida, Magnetic-field-induced shape recovery by reverse phase transformation, Nature 439 (2006) 957–960.

[34] T. Krenke, E. Duman, M. Acet, E.F. Wassermann, X. Moya, L. Mañosa, A. Planes, E. Suard, B. Ouladdiaf, Magnetic superelasticity and inverse magnetocaloric effect in Ni-Mn-In, Phys. Rev. B. 75 (2007) 104414.

[35] H.E. Karaca, I. Karaman, B. Basaran, D.C. Lagoudas, Y.I. Chumlyakov, H.J. Maier, On the stress-assisted magnetic-field-induced phase transformation in Ni2MnGa ferromagnetic shape memory alloys, Acta Mater 55 (2007) 4253–4269.

[36] J.A. Monroe, J. Cruz-Perez, C. Yegin, I. Karaman, A.B. Geltmacher, R.K. Everett, R. Kainuma, Magnetic response of porous NiCoMnSn metamagnetic shape memory alloys fabricated using solid-state replication, Scr. Mater. 67 (2012) 116–119.

[37] J.A. Monroe, I. Karaman, B. Basaran, W. Ito, R.Y. Umetsu, R. Kainuma, K. Koyama, Y.I. Chumlyakov, Direct measurement of large reversible magnetic-field-induced strain in Ni–Co–Mn–In metamagnetic shape memory alloys, Acta Mater 60 (2012) 6883–6891.

[38] S. Rios, D. Bufford, I. Karaman, H. Wang, X. Zhang, Magnetic field induced phase transformation in polycrystalline NiCoMnAl thin films, Appl. Phys. Lett. 103 (2013) 132404.

[39] N.M. Bruno, C. Yegin, I. Karaman, J.-H. Chen, J.H. Ross, J. Liu, J. Li, The effect of heat treatments on Ni43Mn42Co4Sn11 meta-magnetic shape memory alloys for magnetic refrigeration, Acta Mater 74 (2014) 66–84.

[40] K. Haldar, D.C. Lagoudas, I. Karaman, Magnetic field-induced martensitic phase transformation in magnetic shape memory alloys: Modeling and experiments, J. Mech. Phys. Solids. 69 (2014) 33–66.

[41] P.J. Stonaha, M.E. Manley, N.M. Bruno, I. Karaman, R. Arroyave, N. Singh, D.L. Abernathy, S. Chi, Lattice vibrations boost demagnetization entropy in a shape-memory alloy, Phys. Rev. B. 92 (2015) 140406.

[42] B. Emre, N.M. Bruno, S. Yuce Emre, I. Karaman, Effect of niobium addition on the martensitic transformation and magnetocaloric effect in low hysteresis NiCoMnSn magnetic shape memory alloys, Appl. Phys. Lett. 105 (2014) 231910.

[43] R. Santamarta, A. Evirgen, A.M. Perez-Sierra, J. Pons, E. Cesari, I. Karaman, R.D. Noebe, Effect of Thermal Treatments on Ni–Mn–Ga and Ni-Rich Ni–Ti–Hf/Zr High-Temperature Shape Memory Alloys, Shape Mem. Superelasticity 1 (2015) 418–428.

[44] V.R. Guiza-Arguello, J.A. Monroe, I. Karaman, M.S. Hahn, Cytocompatibility evaluation of NiMnSn meta-magnetic shape memory alloys for biomedical applications, J. Biomed. Mater. Res. B Appl. Biomater. 104 (2016) 853–863.

[45] N.M. Bruno, Y.J. Huang, C.L. Dennis, J.G. Li, R.D. Shull, J.H. Ross, Y.I. Chumlyakov, I. Karaman, Effect of grain constraint on the field requirements for magnetocaloric effect in Ni45Co5Mn40Sn10 melt-spun ribbons, J. Appl. Phys. 120 (2016) 075101.

[46] N.M. Bruno, D. Salas, S. Wang, I.V. Roshchin, R. Santamarta, R. Arroyave, T. Duong, Y.I. Chumlyakov, I. Karaman, On the microstructural origins of martensitic transformation arrest in a NiCoMnIn magnetic shape memory alloy, Acta Mater 142 (2018) 95–106.

[47] D. Salas, O. Eliseeva, Y. Wang, T. Duong, Y.I. Chumlyakov, Y. Ren, R. Arroyave, I. Karaman, Effects of composition and crystallographic ordering on the ferromagnetic transition in NiCoMnIn magnetic shape memory alloys, Acta Mater 166 (2019) 630–637.

[48] H.E. Karaca, I. Karaman, B. Basaran, Y. Ren, Y.I. Chumlyakov, H.J. Maier, Magnetic Field-Induced Phase Transformation in NiMnCoIn Magnetic Shape-Memory Alloys-A New Actuation Mechanism with Large Work Output, Adv. Funct. Mater. 19 (2009) 983–998.

[49] J.A. Monroe, J.E. Raymond, X. Xu, M. Nagasako, R. Kainuma, Y.I. Chumlyakov, R. Arroyave, I. Karaman, Multiple ferroic glasses via ordering, Acta Mater 101 (2015) 107–115.

[50] K. Ullakko, J.K. Huang, C. Kantner, R.C. O'Handley, V.V. Kokorin, Large magnetic-field-induced strains in Ni2MnGa single crystals, Appl. Phys. Lett. 69 (1996) 1966–1968.

[51] I. Karaman, H.E. Karaca, B. Basaran, D.C. Lagoudas, Y.I. Chumlyakov, H.J. Maier, Stress-assisted reversible magnetic field-induced phase transformation in Ni2MnGa magnetic shape memory alloys, Scr. Mater. 55 (2006) 403–406.

[52] J. Nogués, I.K. Schuller, Exchange bias, J. Magn. Magn. Mater. 192 (1999) 203–232.

[53] Z. Li, C. Jing, J. Chen, S. Yuan, S. Cao, J. Zhang, Observation of exchange bias in the martensitic state of Ni50Mn36Sn14 Heusler alloy, Appl. Phys. Lett. 91 (2007) 112505.

[54] M. Khan, I. Dubenko, S. Stadler, N. Ali, Exchange bias behavior in Ni–Mn–Sb Heusler alloys, Appl. Phys. Lett. 91 (2007) 072510.

[55] K. Ullakko, J.K. Huang, V.V. Kokorin, R.C. O'Handley, Magnetically controlled shape memory effect in Ni2MnGa intermetallics, Scr. Mater. 36 (1997) 1133–1138.

[56] I. Suorsa, E. Pagounis, K. Ullakko, Magnetic shape memory actuator performance, J. Magn. Magn. Mater. 272–276 (2004) 2029–2030.

[57] H.E. Karaca, I. Karaman, B. Basaran, Y.I. Chumlyakov, H.J. Maier, Magnetic field and stress induced martensite reorientation in NiMnGa ferromagnetic shape memory alloy single crystals, Acta Mater 54 (2006) 233–245.

[58] M.A. Marioni, R.C. O'Handley, S.M. Allen, S.R. Hall, D.I. Paul, M.L. Richard, J. Feuchtwanger, B.W. Peterson, J.M. Chambers, R. Techapiesancharoenkij, The ferromagnetic shape-memory effect in Ni–Mn–Ga, J. Magn. Magn. Mater. 290–291 (2005) 35–41.

[59] N. Sarawate, M. Dapino, Experimental characterization of the sensor effect in ferromagnetic shape memory Ni–Mn–Ga, Appl. Phys. Lett. 88 (2006) 121923.

[60] T. Krenke, E. Duman, M. Acet, E.F. Wassermann, X. Moya, L. Mañosa, A. Planes, Inverse magnetocaloric effect in ferromagnetic Ni–Mn–Sn alloys, Nat. Mater. 4 (2005) 450–454.

[61] K.A. GschneidnerJr, V.K. Pecharsky, A.O. Tsokol, Recent developments in magnetocaloric materials, Rep. Prog. Phys. 68 (2005) 1479.
[62] E. Brück, Developments in magnetocaloric refrigeration, J. Phys. Appl. Phys. 38 (2005) R381–R391.
[63] V.K. Sharma, M.K. Chattopadhyay, S.B. Roy, Large inverse magnetocaloric effect in Ni 50 Mn 34 In 16, J. Phys. Appl. Phys. 40 (2007) 1869.
[64] A.K. Pathak, M. Khan, I. Dubenko, S. Stadler, N. Ali, Large magnetic entropy change in Ni50Mn50−XInX Heusler alloys, Appl. Phys. Lett. 90 (2007) 262504.
[65] A. Planes, L. Mañosa, M. Acet, Magnetocaloric effect and its relation to shape-memory properties in ferromagnetic Heusler alloys, J. Phys. Condens. Matter. 21 (2009) 233201.
[66] J.M. Barandiarán, V.A. Chernenko, P. Lázpita, J. Gutiérrez, J. Feuchtwanger, Effect of martensitic transformation and magnetic field on transport properties of Ni-Mn-Ga and Ni-Fe-Ga Heusler alloys, Phys. Rev. B. 80 (2009) 104404.
[67] J. Liu, T. Gottschall, K.P. Skokov, J.D. Moore, O. Gutfleisch, Giant magnetocaloric effect driven by structural transitions, Nat. Mater. 11 (2012) 620–626.
[68] Y. Song, K. Preet Bhatti, V. Srivastava, C. Leighton, R.D. James, Thermodynamics of energy conversion via first order phase transformation in low hysteresis magnetic materials, Energy Environ. Sci. 6 (2013) 1315–1327.
[69] N. Singh, R. Arróyave, Magnetocaloric effects in Ni-Mn-Ga-Fe alloys using Monte Carlo simulations, J. Appl. Phys. 113 (2013) 183904.
[70] J.-H. Chen, N.M. Bruno, I. Karaman, Y. Huang, J. Li, J.H. Ross, Calorimetric and magnetic study for Ni50Mn36In14 and relative cooling power in paramagnetic inverse magnetocaloric systems, J. Appl. Phys. 116 (2014) 203901.
[71] J.-H. Chen, N.M. Bruno, I. Karaman, Y. Huang, J. Li, J.H. Ross Jr, Direct measure of giant magnetocaloric entropy contributions in Ni–Mn–In, Acta Mater 105 (2016) 176–181.
[72] T.D. Brown, I. Karaman, P.J. Shamberger, Impact of cycle-hysteresis interactions on the performance of giant magnetocaloric effect refrigerants, Mater. Res. Express. 3 (2016) 074001.
[73] B. Emre, S. Yuce, N.M. Bruno, I. Karaman, Martensitic transformation and magnetocaloric properties of NiCoMnSn magnetic shape memory alloys, Intermetallics 106 (2019) 65–70.
[74] P. Müllner, V.A. Chernenko, G. Kostorz, Stress-induced twin rearrangement resulting in change of magnetization in a Ni–Mn–Ga ferromagnetic martensite, Scr. Mater. 49 (2003) 129–133.
[75] N.E. Barta, I. Karaman, Embedded magnetic shape memory sensory particles in lightweight composites for crack detection, Mater. Sci. Eng. A. 751 (2019) 201–213.
[76] B.M. Wang, L. Wang, Y. Liu, B.C. Zhao, Y. Zhao, Y. Yang, H. Zhang, Strong thermal-history-dependent magnetoresistance behavior in Ni49.5Mn34.5In16, J. Appl. Phys. 106 (2009) 063909.
[77] L. Porcar, D. Bourgault, P. Courtois, Large piezoresistance and magnetoresistance effects on Ni45Co5Mn37.5In12.5 single crystal, Appl. Phys. Lett. 100 (2012) 152405.
[78] S. Sarkar, X. Ren, K. Otsuka, Evidence for Strain Glass in the Ferroelastic–Martensitic System Ti50-xNi50+x, Phys. Rev. Lett. 95 (2005) 205702.
[79] Y. Wang, C. Huang, J. Gao, S. Yang, X. Ding, X. Song, X. Ren, Evidence for ferromagnetic strain glass in Ni-Co-Mn-Ga Heusler alloy system, Appl. Phys. Lett. 101 (2012) 101913.
[80] S. Kustov, D. Salas, E. Cesari, R. Santamarta, D. Mari, J. Van Humbeeck, Strain–Glass Revisited, Mater. Sci. Forum. 738–739 (2013) 274–275.
[81] X. Ren, Strain glass and ferroic glass – Unusual properties from glassy nano–domains, Phys. Status Solidi B. 251 (2014) 1982–1992.
[82] P.J. Stonaha, I. Karaman, R. Arroyave, D. Salas, N.M. Bruno, Y. Wang, M.F. Chisholm, S. Chi, D.L. Abernathy, Y.I. Chumlyakov, M.E. Manley, Glassy Phonon Heralds a Strain Glass State in a Shape Memory Alloy, Phys. Rev. Lett. 120 (2018) 245701.
[83] K. Binder, A.P. Young, Spin glasses: Experimental facts, theoretical concepts, and open questions, Rev. Mod. Phys. 58 (1986) 801.
[84] S. Morito, T. Kakeshita, K. Hirata, K. Otsuka, Magnetic and martensitic transformations in Ni50AlxMn50−x alloys, Acta Mater 46 (1998) 5377–5384.
[85] S. Chatterjee, S. Giri, S.K. De, S. Majumdar, Reentrant-spin-glass state in Ni2Mn1.36Sn0.64 shape-memory alloy, Phys. Rev. B. 79 (2009) 092410.
[86] W. Ito, M. Nagasako, R.Y. Umetsu, R. Kainuma, T. Kanomata, K. Ishida, Atomic ordering and magnetic properties in the Ni45Co5Mn36.7In13.3 metamagnetic shape memory alloy, Appl. Phys. Lett. 93 (2008) 232503.
[87] S. Kustov, M.L. Corró, J. Pons, E. Cesari, Entropy change and effect of magnetic field on martensitic transformation in a metamagnetic Ni–Co–Mn–In shape memory alloy, Appl. Phys. Lett. 94 (2009) 191901.
[88] T. Graf, C. Felser, S.S.P. Parkin, Simple rules for the understanding of Heusler compounds, Prog. Solid State Chem. 39 (2011) 1–50.
[89] A. Sozinov, A.A. Likhachev, N. Lanska, K. Ullakko, Giant magnetic-field-induced strain in NiMnGa seven-layered martensitic phase, Appl. Phys. Lett. 80 (2002) 1746–1748.
[90] Y. Sutou, Y. Imano, N. Koeda, T. Omori, R. Kainuma, K. Ishida, K. Oikawa, Magnetic and martensitic transformations of NiMnX(X=In,Sn,Sb) ferromagnetic shape memory alloys, Appl. Phys. Lett. 85 (2004) 4358–4360.
[91] J. Pons, V.A. Chernenko, R. Santamarta, E. Cesari, Crystal structure of martensitic phases in Ni–Mn–Ga shape memory alloys, Acta Mater 48 (2000) 3027–3038.
[92] W. Ito, Y. Imano, R. Kainuma, Y. Sutou, K. Oikawa, K. Ishida, Martensitic and Magnetic Transformation Behaviors in Heusler-Type NiMnIn and NiCoMnIn Metamagnetic Shape Memory Alloys, Metall. Mater. Trans. A. 38 (2007) 759–766.
[93] K. Adachi, C.M. Wayman, Transformation behavior of nearly stoichiometric Ni-Mn alloys, Metall. Trans. A 16 (1985) 1567–1579.
[94] M. Zarinejad, Y. Liu, Dependence of Transformation Temperatures of Ni-Ti-based Shape-Memory Alloys on the Number and Concentration of Valence Electrons, Adv. Funct. Mater. 18 (2008) 2789–2794.
[95] T. Krenke, M. Acet, E.F. Wassermann, X. Moya, L. Mañosa, A. Planes, Ferromagnetism in the austenitic and martensitic states of Ni-Mn-In alloys, Phys. Rev. B. 73 (2006) 174413.
[96] T.B. Massalski, Comments Concerning Some Features of Phase Diagrams and Phase Transformations, Mater. Trans. 51 (2010) 583–596.
[97] V.D. Buchelnikov, P. Entel, S.V. Taskaev, V.V. Sokolovskiy, A. Hucht, M. Ogura, H. Akai, M.E. Gruner, S.K. Nayak, Monte Carlo study of the influence of antiferromagnetic exchange interactions on the phase transitions of ferromagnetic Ni-Mn-X alloys (X=In,Sn,Sb), Phys. Rev. B. 78 (2008) 184427.
[98] R.Y. Umetsu, W. Ito, K. Ito, K. Koyama, A. Fujita, K. Oikawa, T. Kanomata, R. Kainuma, K. Ishida, Anomaly in entropy change between parent and martensite phases in the Ni50Mn34In16 Heusler alloy, Scr. Mater. 60 (2009) 25–28.
[99] J.I. Pérez-Landazábal, V. Recarte, V. Sánchez-Alarcos, M.J. Ruiz, E. Cesari, Outstanding role of the magnetic entropy in arrested austenite in an ordered Ni45Mn36.7In13.3Co5 metamagnetic shape memory alloy, Scr. Mater. 168 (2019) 91–95.
[100] V. Sánchez-Alarcos, V. Recarte, J.I. Pérez-Landazábal, G.J. Cuello, Correlation between atomic order and the characteristics of the structural and magnetic transformations in Ni–Mn–Ga shape memory alloys, Acta Mater 55 (2007) 3883–3889.
[101] P. Neibecker, M. Leitner, G. Benka, W. Petry, Increasing the achievable state of order in Ni-based Heusler alloys via quenched-in vacancies, Appl. Phys. Lett. 105 (2014) 261904.
[102] V. Sánchez-Alarcos, J.I. Pérez-Landazábal, V. Recarte, I. Lucia, J. Vélez, J.A. Rodríguez-Velamazán, Effect of high-temperature quenching on the magnetostructural transformations and the long-range atomic order of Ni–Mn–Sn and Ni–Mn–Sb metamagnetic shape memory alloys, Acta Mater 61 (2013) 4676–4682.
[103] K. Oikawa, T. Ota, T. Ohmori, Y. Tanaka, H. Morito, A. Fujita, R. Kainuma, K. Fukamichi, K. Ishida, Magnetic and martensitic phase transitions in ferromagnetic Ni–Ga–Fe shape memory alloys, Appl. Phys. Lett. 81 (2002) 5201–5203.
[104] V. Sánchez-Alarcos, J.I. Pérez-Landazábal, V. Recarte, J.A. Rodríguez-Velamazán, V.A. Chernenko, Effect of atomic order on the martensitic and magnetic transformations in Ni–Mn–Ga ferromagnetic shape memory alloys, J. Phys. Condens. Matter. 22 (2010) 166001.
[105] Y. Wang, D. Salas, T.C. Duong, B. Medasani, A. Talapatra, Y. Ren, Y.I. Chumlyakov, I. Karaman, R. Arróyave, On the fast kinetics of B2–L21 ordering in Ni-Co-Mn-In metamagnetic shape memory alloys, J. Alloys Compd. 781 (2019) 479–489.
[106] V. Hardy, S. Hébert, A. Maignan, C. Martin, M. Hervieu, B. Raveau, Staircase effect in metamagnetic transitions of charge and orbitally ordered manganites, J. Magn. Magn. Mater. 264 (2003) 183–191.
[107] X.M. Sun, D.Y. Cong, K.-D. Liss, Y.H. Qu, L. Ma, H.L. Suo, Y.D. Wang, Origin of anomalous cryogenic magnetic behavior in a Ni-Mn-based magnetic shape memory alloy, Appl. Phys. Lett. 110 (2017) 132402.
[108] V.K. Pecharsky Jr, K.A. Gschneidner, Giant Magnetocaloric Effect in Gd5(Si2Ge2), Phys. Rev. Lett. 78 (1997) 4494–4497.
[109] A. Planes, L. Manosa, E. Vives, J. Rodriguez-Carvajal, M. Morin, G. Guenin, J.L. Macqueron, Neutron diffraction study of long-range atomic order in Cu-Zn-Al shape memory alloys, J. Phys. Condens. Matter. 4 (1992) 553–559.
[110] T. Krenke, M. Acet, E.F. Wassermann, X. Moya, L. Mañosa, A. Planes, Martensitic transitions and the nature of ferromagnetism in the austenitic and martensitic states of Ni-Mn-Sn alloys, Phys. Rev. B. 72 (2005) 014412.
[111] P. Scherrer, Bestimmung der Größe und der inneren Struktur von Kolloidteilchen mittels Röntgenstrahlen, Gött. Nachrichten Ges. J. 2 (1918) 98.
[112] A.L. Patterson, The Scherrer Formula for X-Ray Particle Size Determination, Phys. Rev. 56 (1939) 978–982.
[113] J.I. Langford, A.J.C. Wilson, Scherrer after sixty years: A survey and some new results in the determination of crystallite size, J. Appl. Crystallogr. 11 (1978) 102–113.
[114] A. Evirgen, I. Karaman, R. Santamarta, J. Pons, R.D. Noebe, Microstructural characterization and shape memory characteristics of the Ni50.3Ti34.7Hf15 shape memory alloy, Acta Mater 83 (2015) 48–60.
[115] T. Krenke, X. Moya, S. Aksoy, M. Acet, P. Entel, Ll. Mañosa, A. Planes, Y. Elerman, A. Yücel, E.F. Wassermann, Electronic aspects of the martensitic transition in Ni–Mn based Heusler alloys, J. Magn. Magn. Mater. 310 (2007) 2788–2789.
[116] V.K. Sharma, M.K. Chattopadhyay, S.B. Roy, Kinetic arrest of the first order austenite to martensite phase transition in Ni50Mn34In16: dc magnetization studies, Phys. Rev. B. 76 (2007) 140401.
[117] C. Seguí, E. Cesari, Contributions to the Transformation Entropy Change and Influencing Factors in Metamagnetic Ni-Co-Mn-Ga Shape Memory Alloys, Entropy 16 (2014) 5560–5574.
[118] Y. Wang, D. Salas, B. Medasani, P. Entel, I. Karaman, R. Arróyave, T.C. Duong, First-Principles Characterization of Equilibrium Vacancy Concentration in Metamagnetic Shape Memory Alloys: An Example of Ni2MnGa, Phys. Status Solidi B. 255 (2018) 1700523.
[119] J.J. Gilman, R.W. Cumberland, R.B. Kaner, Design of hard crystals, Int. J. Refract. Met. Hard Mater. 24 (2006) 1–5.

[120] T. Miyamoto, M. Nagasako, R. Kainuma, Phase equilibria in the Ni–Mn–In alloy system, J. Alloys Compd. 549 (2013) 57–63.
[121] K. Niitsu, K. Minakuchi, X. Xu, M. Nagasako, I. Ohnuma, T. Tanigaki, Y. Murakami, D. Shindo, R. Kainuma, Atomic-resolution evaluation of microsegregation and degree of atomic order at antiphase boundaries in Ni50Mn20In30 Heusler alloy, Acta Mater 122 (2017) 166–177.
[122] A. Çakır, M. Acet, M. Farle, Shell-ferromagnetism of nano-Heuslers generated by segregation under magnetic field, Sci. Rep. 6 (2016) 28931.
[123] F. Scheibel, D. Spoddig, R. Meckenstock, T. Gottschall, A. Çakır, T. Krenke, M. Farle, O. Gutfleisch, M. Acet, Room-temperature five-tesla coercivity of a rare-earth-free shell-ferromagnet, Appl. Phys. Lett. 110 (2017) 192406.
[124] A. Çakır, M. Acet, U. Wiedwald, T. Krenke, M. Farle, Shell-ferromagnetic precipitation in martensitic off-stoichiometric Ni-Mn-In Heusler alloys produced by temper-annealing under magnetic field, Acta Mater 127 (2017) 117–123.
[125] E. Hornbogen, The effect of variables on martensitic transformation temperatures, Acta Metall 33 (1985) 595–601.
[126] E.Yu. Panchenko, Yu.I. Chumlyakov, I.V. Kireeva, A.V. Ovsyannikov, H. Sehitoglu, I. Karaman, Y.H.J. Maier, Effect of disperse Ti3N4 particles on the martensitic transformations in titanium nickelide single crystals, Phys. Met. Metallogr. 106 (2008) 577–589.
[127] H.C. Fogedby, O.G. Mouritsen, Lifshitz-Allen-Cahn domain-growth kinetics of Ising models with conserved density, Phys. Rev. B. 37 (1988) 5962–5965.
[128] Image J, (https://imagej.nih.gov/ij/).
[129] K. Binder, Phase Transitions in Reduced Geometry, Annu. Rev. Phys. Chem. 43 (1992) 33–59.
[130] D. Michels, C.E. Krill III, R. Birringer, Grain-size-dependent Curie transition in nanocrystalline Gd: the influence of interface stress, J. Magn. Magn. Mater. 250 (2002) 203–211.
[131] J.M. Yeomans, in: Statistical Mechanics of Phase Transitions, Oxford University Press, Oxford, 1992, pp. 33–49.
[132] A.L. Roitburd, On the thermodynamics of martensite nucleation, Mater. Sci. Eng. A. 127 (1990) 229–238.
[133] V.A. L'vov, E. Cesari, J.I. Pérez-Landazábal, V. Recarte, J. Torrens-Serra, Magnetically driven magnetostructural transformations of shape memory alloys, J. Phys. Appl. Phys. 49 (2016) 095002.
[134] G.B. Olson, M. Cohen, A general mechanism of martensitic nucleation: Part I. General concepts and the FCC → HCP transformation, Metall. Trans. A. 7 (1976) 1897–1904.
[135] Z. Zhang, R.D. James, S. Müller, Energy barriers and hysteresis in martensitic phase transformations, Acta Mater 57 (2009) 4332–4352.
[136] R.C. O'Handley, D.I. Paul, M. Marioni, C.P. Henry, M. Richard, P.G. Tello, S.M. Allen, Micromagnetics and micromechanics of Ni-Mn-Ga actuation, J. Phys. IV Proc. 112 (2003) 973–976.